RICE UNIVERSITY

Evidence for Impulsive Heating of Active Region Coronal Loops

by

Jeffrey Reep

A THESIS SUBMITTED

IN PARTIAL FULFILLMENT OF THE

REQUIREMENTS FOR THE DEGREE

MASTER OF SCIENCE

APPROVED, THESIS COMMITTEE:

Stephen Bradshaw, Chair
Assistant Professor of Physics & Astronomy

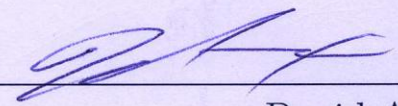

David Alexander
Professor of Physics & Astronomy

Karl Ecklund
Assistant Professor of Physics & Astronomy

Houston, Texas

May, 2012

ABSTRACT

Evidence for Impulsive Heating of Active Region Coronal Loops

by

Jeffrey Reep

We present observational and numerical evidence supporting the theory of impulsive heating of the solar corona. We have run numerical simulations solving the hydrodynamic equations for plasma confined to a magnetic flux tube, for the two distinct cases of steady and impulsive heating. We find that steady heating cannot explain the observed amount of low-temperature plasma in active regions on the sun. The results for impulsive heating closely match those of the observations. The ratio of heating time to cooling time predominantly determines the observed temperature distribution of the plasma. We have also identified an observational bias in calculating intensities of spectral lines in previous studies, which causes an under-estimation of low-temperature plasma. We predict Doppler shifts in the observed line emission that are in agreement with observations, and which may serve as a diagnostic of the strength of heating. We conclude that impulsive heating of active region coronal loops is more likely than steady heating.

Table of Contents

List of Figures

List of Tables

1 Introduction

1.1 Early Studies of the Solar Corona

The solar corona, known since ancient times, has presented many intriguing problems for physicists over the long history of studying it. For thousands of years, the only time when people could see, and thus study, the corona was during solar eclipses. The earliest reliably documented eclipses come from the Chinese classic *The Annals of Lu*, recording eclipses from 720 to 495 B.C. (other works reference a Chinese observation from 2137 B.C. and a Babylonian observation from 1063 B.C., although these are disputed; Mitchell 1932 [48]; Golub & Pasachoff 2010 [31]). Solar eclipses occur when the moon, which has the fortuitous feature of being roughly the same angular size on the sky as the sun, moves between the Earth and the sun, thus blocking out the light from the sun's photosphere. The light that remains is scattered by the upper atmosphere of the sun, in the tenuous region known as the corona (Latin for crown). Figure 1-1 shows the most recent total solar eclipse, which occurred on 11 July 2010 (the next will not be until 13 November 2012); the corona is clearly visible as a white ring around the center of the sun, which is blocked by the moon.

Figure 1-1: The most recent total solar eclipse, 11 July 2010, observed over the south Pacific, near the coast of Tahiti. The corona of the sun, clearly visible here, appears as a white ring around the center of the sun, which is blocked by the moon. Courtesy of Dr. Patricia Reiff, Rice University.

Modern scientific study of the corona began in the mid-nineteenth century (see chapter 2 of Golub & Pasachoff 2010 [31]). The first major problem for physics that the corona presented was a bright spectral line (at roughly 5303 Å, in the green part of the visible spectrum), first noticed during the eclipse of 1869, and studied for many years thereafter (see Young 1872 [82] for an early history of this emission line). The line presented the problem that it did not appear to be emitted by any known element, and that the height of emission above the solar surface seemed far too high. Defining the scale height h as the distance over which the pressure falls by a factor of $1/e$, we find that h is proportional to the temperature and inversely proportional to the molecule's mass. The large observed height of the emission thus implied that either the temperature of the gas was extremely high or the mass of the atom was extremely small (less than hydrogen). Based on the example of the recently discovered helium, they named this "newly discovered element" coronium. In subsequent eclipses, many more of these unknown coronium-type lines would be discovered.

In 1930, Bernard Lyot invented a device called the coronagraph, which essentially creates an artificial eclipse for a telescope by blocking out the light from the photosphere (Lyot 1930 [43]). This landmark

invention allowed astronomers to study the corona without the need to wait for an eclipse, and without the short time window provided by an eclipse. In 1939, making use of his coronagraph, Lyot reported that the 5303 Å coronium line had a mean width of about 0.8 Å, with a maximum value of 1.2 Å, significantly broader than any nearby lines (Lyot 1939 [44]). Assuming the width is due to thermal broadening, the temperature of the gas would have to be significantly higher than the sun's surface temperature of about 5,800 K (in the 1939 paper, Lyot did not calculate the temperature since he did not know the mass of coronium, but if we use the mass of an iron atom, the gas temperature would have be around 2.5 MK).

Meanwhile, astronomers looking at the spectrum of a nova, 1925 RR Pictoris, observed two strong spectral lines (at 5723 Å and 6087 Å) that had never been seen before, along with numerous (weaker) unidentified lines (Jones 1933 [34]). While studying forbidden transitions of manganese and iron, the spectroscopist Bowen in the mid-1930s managed to identify three of the weaker lines (at 4968.1 Å, 5148.5Å, and 5176.3 Å) as forbidden transitions of [Fe VI] (Bowen 1935 [7]).

Before proceeding, a few notes about spectroscopy and the notation are necessary. The notation "Fe VI" refers to an iron ion which

has lost 5 of its shell electrons. In spectroscopic notation, we write the element name, X, followed by a Roman numeral, indicating how many electrons have been lost. Roman numeral I corresponds to the neutral atom, II corresponds to one lost shell electron, III means two lost electrons, *etc.* For example, H I refers to neutral hydrogen, while H II refers to singly ionized hydrogen, and there is no such thing as H III or higher, since neutral hydrogen only has one shell electron. When we say "forbidden transitions," we are not referring to transitions which are impossible; rather, by forbidden, we mean that they are transitions that do not follow the classical selection rules of quantum mechanics (see chapter 10 of Rybicki and Lightman 1979 [59] for more information). Finally, when the ion name is enclosed in brackets, like [Fe VI], the brackets indicate that the spectral line to which we refer is forbidden.

Following the example of the [Fe VI] lines, Bowen and Edlén realized that to identify the two strong unknown lines in RR Pictoris, they would need to analyze more highly ionized ions. Indeed, in 1939, they identified the two strong lines as both being caused by [Fe VII] (Bowen & Edlén 1939 [8]). Actually, the full truth is that the 6087 Å line comes from a blend of [Fe VII] and [Ca V]. The correct identification of these

lines as coming from highly charged ions led solar physicists to the next step of solving their coronium puzzle.

In 1939, following some of Edlén's earlier laboratory work (Edlén 1937 [23]), Grotrian noticed that the 6374 Å line (the so-called coronal "red line") and the 7892 Å line (a coronal line in the near infrared) corresponded to forbidden transitions of doublet states of [Fe X] and [Fe XI], respectively (Grotrian 1939 [32]). Shortly thereafter, in 1941, Edlén published a paper identifying 19 of the 24 known coronal lines, including the identification of the 5303 Å coronium green line as an [Fe XIV] transition, $3p^2 P_{3/2} -^2 P_{1/2}$ (Edlén 1941 [24]). The problem had been solved, without the need to hypothesize a new element!

Unfortunately, while the problem of identifying the coronium lines was over, the existence and widths of the lines led to a new problem. Quoting Hunter (1942 [33]): "Turning now to the physical conditions required by Edlén's proposals, the most striking fact is the enormous energy required to strip the atoms of iron, nickel and calcium of so many electrons. In this connexion it is perhaps significant that Lyot, in order to account for the width of the coronal lines by pure thermal motion, found that a temperature of 660,000° K. would be needed if the emitting particles were as heavy as oxygen atoms. Recalculating to iron

atoms, 3-5 times heavier, a coronal temperature of 2,300,000° K. must be postulated; and at this temperature an atom in thermal equilibrium with its neighbours will have an average translational energy of more than 300 electron volts. What may be the physical meaning of a coronal 'temperature' of more than two million degrees is as yet unknown..."

Today, it is readily accepted that the corona has a temperature above a million degrees Kelvin. It is worth noting that due to the extremely low density, the energy density in the corona is significantly less than the 5,800 K surface (taking the densities to be 10^9 cm^{-3} in the corona and 10^{17} cm^{-3} in the photosphere, the energy densities are roughly 10^{-1} and 10^5 erg cm^{-3}, respectively). Nevertheless, the energy per particle in the corona is more than 100 times greater than that of the surface of the sun. To reach such high temperatures, even with the significant drop in density, there must be some sort of heating mechanism that releases energy into the atmosphere. The work reported in this thesis seeks to address how the corona might form and be maintained by one such heating mechanism: impulsive nanoflare heating (see below for more information).

1.2 The Structure of the Atmosphere

The solar atmosphere is divided into four distinct regions (see figure 1-2). The lowest, the photosphere, is what we traditionally call the surface of the sun. It is defined as the region where the optical depth attains the value 2/3, which corresponds to being opaque to our eyes. The photosphere has an effective temperature of about 5,800 K, although sunspots can be as low as 4,000 K. Above the photosphere is the chromosphere, often characterized by its many emission lines. The temperature here rises to around 20,000 K, so that some atoms become ionized, although there are still many neutral atoms around. Phenomena like prominences and spicules rise up from the chromosphere. Above the chromosphere is the transition region, where the density drops and the temperature rises sharply in a very thin region. Finally, the hottest region is known as the corona, the focus of the current work. Phenomena like solar flares and coronal mass ejections originate here (flares also are observed in the chromosphere), while the solar wind escapes from areas called coronal holes, where the magnetic field lines extend far into interplanetary space. Chapter 7 of Alexander (2009 [1]) provides a good introduction to the various regions and the phenomena occurring therein.

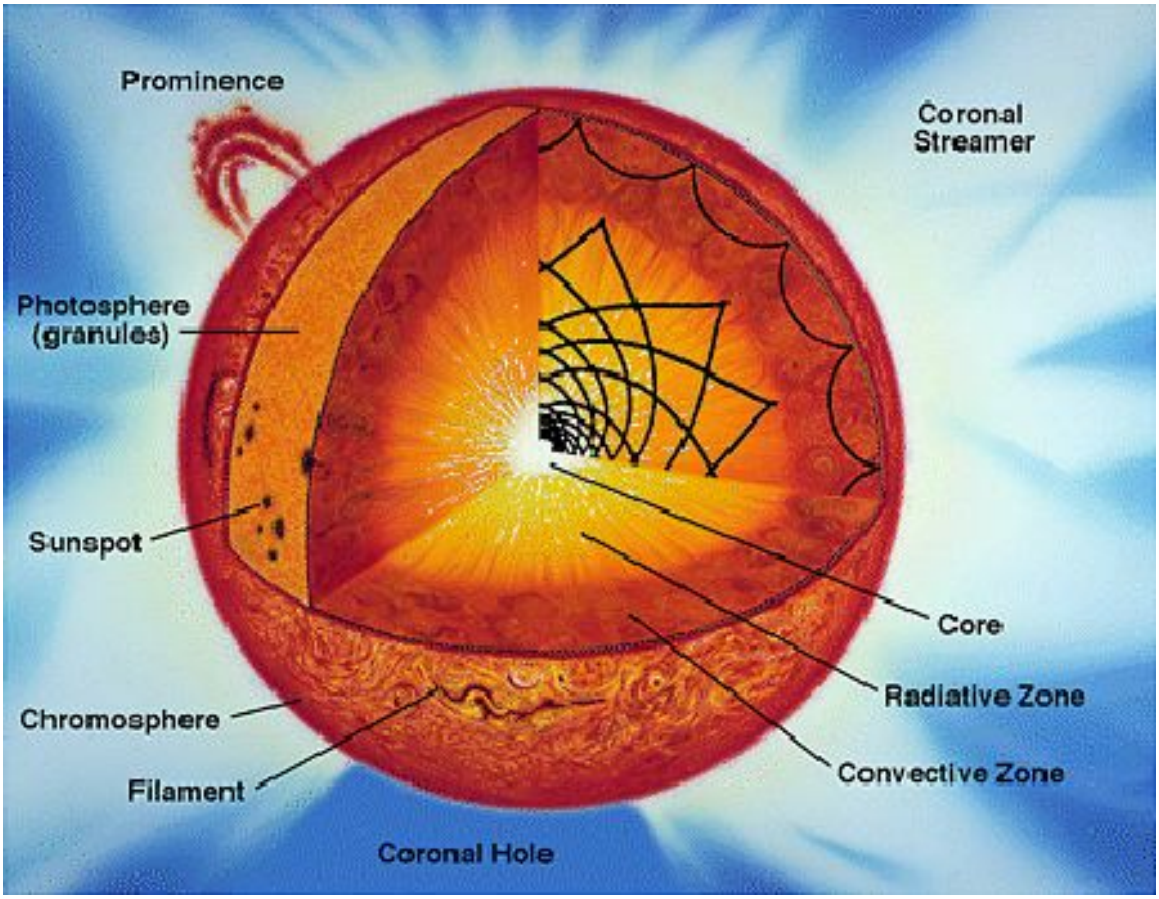

Figure 1-2: The various regions of the sun. The core of the sun is where fusion of hydrogen atoms into helium atoms takes place, powering the sun. Outside the core is the radiation zone, where photons generated in the fusion process in the core slowly make their way outwards. Further out is the convection zone, where hot plasma rises towards the surface. Above that is the photosphere, the surface of the sun as our eyes see it. Above the photosphere is the chromosphere, a region known for having many emission lines of various elements. Then there is a very thin region known as the transition region, where the density falls rapidly and the temperature rises rapidly. Finally, the highest layer of the atmosphere is the tenuous corona, the focus of this work.

A large portion of modern solar physics revolves around explaining the many different processes occurring within the solar corona. The driver of solar coronal activity boils down to the magnetic field; as such, we must try to understand the topology, strength, and spatial and temporal variations of the magnetic field. The area of solar physics concerned with explaining the generation of the magnetic field in the solar interior is known as dynamo theory. Dynamo theory also concerns itself with attempting to explain the solar cycle (an 11-year cycle of activity in the corona). Although it is beyond the scope of the current work, by studying the differential rotation of the sun's surface, the convection in the upper layers, and pressure waves near the surface (helioseismology), researchers are making significant strides in explaining the solar activity cycle. For a comprehensive overview of dynamo theory, see the review by Ossendrijver (2003 [49]).

Without concerning ourselves with how it is generated, we can still make a few important remarks about the magnetic field in the corona. We first take note of the Lorentz force law:

$$\mathbf{F} = q(\mathbf{E} + \frac{\mathbf{v}}{c} \times \mathbf{B}) \tag{1}$$

where $\mathbf{F}$ is the electromagnetic force, q is the particle charge, $\mathbf{E}$ is the electric field, $\mathbf{v}$ is the particle velocity, c is the speed of light in vacuum, and $\mathbf{B}$ is the magnetic field. Note that here, and throughout the current work, we will be using cgs units. For any plasma contained in a magnetic field, we may define the plasma β value as the ratio of gas pressure to magnetic pressure:

$$\beta \equiv \frac{P_{gas}}{P_{mag}} = \frac{8\pi P_{gas}}{B^2} = \frac{16\pi n k_B T}{B^2} \tag{2}$$

where we have taken B to be the magnetic field strength, n to be the number density (and assumed charge neutrality, *i.e.*, that the ion and electron densities are equal, $n_e = n_i$), k_B the Boltzmann constant, and T the temperature (and again, assumed that the ion and electron temperatures are equal). In the corona, we cannot directly measure the field strength (due to the large thermal broadening of lines, Zeeman splitting is essentially impossible to measure) and thus we cannot directly measure the plasma β (new instruments such as the Coronal Multichannel Polarimeter are attempting to overcome this problem; see Tomczyk *et al.* 2008 [65]). However, studies for many years have demonstrated that the coronal $\beta \ll 1$, that is, that the magnetic pressure dominates the gas pressure (see for example Dulk & McLean 1978 [22]; β depends

on height though, see figure 1-3 taken from Gary 2001 [27]). Further, high resolution extreme ultra-violet (EUV) observations of the plasma in the corona from many different satellites (Yohkoh, TRACE, SOHO, Hinode, SDO *etc.*) clearly show the plasma confined to so-called coronal loops, indicating that the magnetic pressure is dominating the gas pressure, acting to confine the gas in narrow magnetic flux tubes. It can also be shown (*e.g.*, Goedbloed & Poedts 2004 [28]) that the thermal conductivity parallel to the magnetic field far exceeds the conductivity perpendicular to the field (by a factor of about 10^8). Thus, since the Lorentz force acts to constrain charged particles to follow magnetic field lines (in the absence of electric fields), and the plasma β is small, we can reasonably conclude that coronal loops are isolated structures with little cross-field interaction and transport.

The basic structure of the corona, then, is the coronal loop, a manifestation of the local field lines. Figure 1-4 (taken by the Solar Dynamics Observatory Atmospheric Imaging Assembly, hereafter SDO-AIA) shows many different coronal loops of many different sizes originating from so-called active regions (see next section for more details). The image was taken in 171 Å EUV light, a signature of plasma at a temperature of roughly 6.3×10^5 K, being emitted by Fe IX ions.

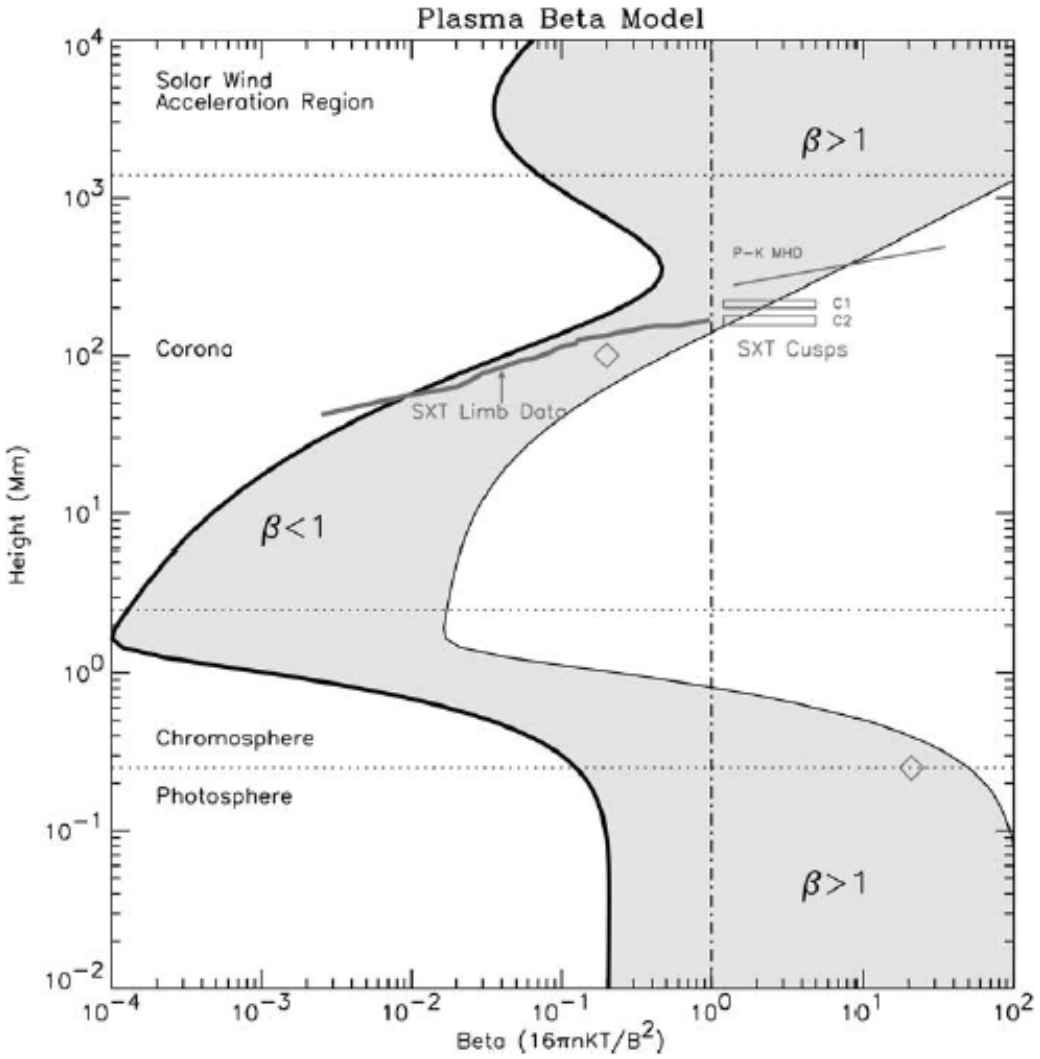

Figure 1-3: The plasma beta as a function of height above the solar surface. The left- and right-hand side limits are for magnetic field lines originating from an active region of 2500 G and a plage of about 150 G, between which most coronal field lines should be contained. See figure 1-2 and the accompanying text for more information on the layers of the sun's atmosphere. Taken from Gary 2001 [27].

Loops can extend over lengths from 10^8 cm on the small side to well over 10^{11} cm. Loop temperatures can vary between 10^5 K to a few 10^7 K in flaring loops. Loop densities have been observed from roughly 10^8 cm^{-3} to over 10^{11} cm^{-3} in the hottest loops (Reale 2010 [57]).

Researchers classify coronal loops in terms of their temperatures, or, correspondingly, their emission of light. For example, Reale (2010 [57]) lists three basic types: cold (10^5 - 10^6 K, seen in UV lines), warm (10^6 - 1.5 $\times 10^6$ K, typically seen in EUV lines), and hot ($> 2 \times 10^6$ K, typically seen in X-rays and hot EUV lines) loops, to which perhaps should be added flaring loops ($\geq 10 \times 10^6$ K). Reale suggests that the different types of loops may be governed by different regimes of physics, and hence the distinctions are not arbitrary.

Coronal loops are often assumed to be semi-circular structures. Loop lengths are then calculated under this assumption using the foot-point to foot-point distance (also assuming the loop is not inclined to the line-of-sight). However, as Reale (2010 [57]) points out, loops often deviate from this shape, and determining their exact lengths can be tricky. For example, the early study of Berton & Sakurai (1985 [6]) found fairly large deviations from semi-circular shapes with apices shifted towards one of the foot-points, which they posit being due to

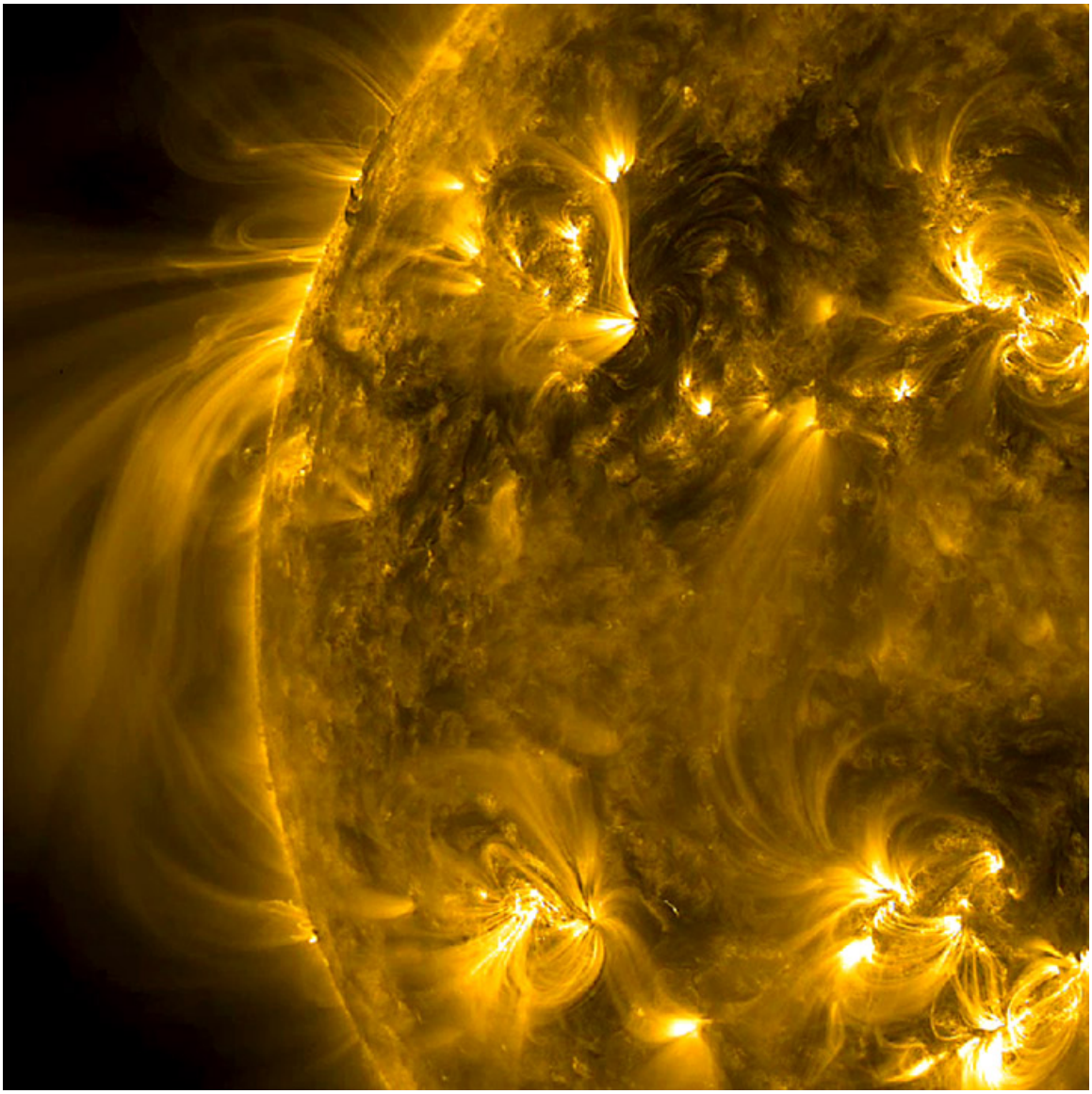

Figure 1-4: EUV image taken by SDO-AIA showing many different coronal loops of many different sizes extending outward from a few different active regions. Notable in this image are the tall loops extending across roughly one third of the solar surface. The image is in 171 Å EUV light, being emitted by Fe IX, at a temperature of roughly 6.3×10^5 K.

one foot-point having a more concentrated magnetic field than the other (a general property of active regions). The Solar TErrestrial RElations Observatory (STEREO, Kaiser *et al.* 2008 [38]) mission is, at the present, giving new insight into the problem: the perspective from each of the STEREO satellites allows observers to reconstruct the three-dimensional geometry of coronal loops (*e.g.*, Feng *et al.* 2007 [26], Aschwanden & Sandman 2010 [5]). The cross-section of coronal loops has been found to have little variation ($< 30\%$) along the length of the loop (Klimchuk *et al.* 1992 [39]); what little variation exists may be due to twisting of magnetic field lines.

We would like to determine the basic structure of coronal loops: are they are single monolithic structures or bundles of many isolated magnetic strands? Whenever higher resolution imaging satellites are launched, they resolve more structure than were visible with older satellites. For example, figure 3 of Del Zanna & Mason (2003 [17]) compares cotemporal images of loops using the Solar and Heliospheric Observatory's Coronal Diagnostic Spectrometer (SOHO-CDS) and the (higher resolution) Transition Region and Coronal Explorer (TRACE). The TRACE images clearly show loop structures that the CDS images fail to resolve (although CDS is a spectrometer which must raster to create

an image, which may affect the resolution). The question then becomes whether our current imaging instruments are resolving the loops or if we are still seeing bundles of many isolated magnetic strands. Winebarger & Warren (2005 [77] found a similar result when comparing Yohkoh Soft X-ray Telescope (SXT) images with TRACE images. If we define a filling factor f as:

$$f \equiv \frac{V_{em}}{V_{res}} \tag{3}$$

where V_{em} is the true volume of emitting plasma, and V_{res} is the volume resolved by an instrument, then observers can use such a number to determine whether we have resolved the basic structure of a coronal loop (a filling factor less than 1 implies unresolved structure). We shall return to methods for calculating the filling factor in practice; for now, we wish to remark that many observers have found a low filling factor indicative of unresolved structure. For example, Di Matteo *et al.* (1999 [20]) found a filling factor of less than 1% using the Normal Incidence X-ray Telescope (NIXT; Golub & Herant 1989 [30]) for plasma between 1 and 3 MK (with a spatial resolution of 1.2" corresponding to about 870 km on the sun). Due diligence is necessary: Di Matteo *et al.* also found

a larger filling factor ($> 10\%$) using the imager Yohkoh-SXT, which has a lower spatial resolution of around 5" (cospatially and cotemporally with the NIXT observations). The discrepancy is likely due to the fact that SXT does not discriminate temperatures very well, being sensitive to a very broad range above about 2 MK. In any case, the results are the same: the filling factor is significantly less than 1, and the loops are not fully resolved.

However, there are others who have argued the opposite: that we have in fact resolved the basic structure of coronal loops. For example, Aschwanden & Nightingale (2005 [4]) observed a large number (roughly 3500) of coronal loops and argue that about 84% of them are isothermal (transverse to the magnetic field), with widths of around 2000 km, well above the resolution threshold. Since there is little cross-field motion between different magnetic strands, separate strands would not necessarily be in thermodynamic equilibrium. Further, as Aschwanden & Nightingale argue, it would be unlikely that adjacent, thermally-isolated strands would maintain the same temperature at all times, and thus isothermality implies that we are seeing a single monolithic structure.

1.3 Active Regions

Regions of significant magnetic activity, active regions, are of particular interest. The brightest areas with many coronal loops emanating outwards in figure 1-4 are examples of active regions. Active regions are generally observed in X-ray and extreme ultraviolet (EUV) light (indicative of high temperatures), appearing brighter than quiet sun regions. As mentioned before, we have no reliable method for measuring the magnetic field strength in the corona; however, we can use Zeeman splitting in the photosphere to measure field strengths there, and we know that generally active regions overlie sunspots or regions that once contained spots.

A large number of coronal loops are located in any given active region. Since the loops emit strongly in X-rays and EUV light, the temperature of these loops must be significant (the majority of emission comes from temperatures around 3-5 MK, although the temperatures in a solar flare can be well over 10 MK). The loops are rooted in lower layers of the atmosphere at the footpoints, where we observe so-called moss regions, at a slightly lower temperature of around 1 MK (Martens *et al.* 2000 [45] argue that the moss emission is from the transition region portion of hot loops, and not smaller, cooler loops). Since active

regions are hotter than the quiet sun regions of the corona (which emit much less strongly in the X-rays and EUV), and since they are regions of strong magnetic activity, the heating mechanisms of the corona must be tied to the magnetic field (see the next section for more). Thus, active regions are a source of interest to study potential coronal heating mechanisms.

Any feasible heating mechanism must explain all observed features of these active region loops. First, the emission from hot X-ray loops in active region cores can remain steady for times exceeding the plasma cooling time (see Rosner *et al.* 1978 [58]). On the other hand, the EUV lines of the same cores show a significant redshift, indicating strong downflows from the loops (*i.e.*, that they are draining due to cooling; for example, Tripathi *et al.* 2009 [66] found downflows of around 60 km/s). We apparently have a contradiction: loops are being steadily heated (so as to maintain the steady X-ray emission) but they are also cooling (causing the draining; *e.g.*, Bradshaw & Cargill 2006 [12]). There is also some evidence that there may be weak blue-wing enhancements of EUV lines (indicating an upflow due to chromospheric ablation; see Martinez-Sykora *et al.* 2011 [46]). This thesis will focus on active region cores and attempts to address these apparently contradictory issues.

1.4 Coronal Loop Heating

Since the strong magnetic field acts to confine the plasma and there is little cross-field motion, the question of how the corona is heated is directly related to how an individual coronal loop is heated. Further, there exists a scaling law (derived in Golub *et al.* 1980 [29]) between the coronal energy density and magnetic field strength, implying that the two are intimately linked. So, the problem becomes how to release the energy stored in the magnetic field and dissipate it locally as heat. There are two commonly suggested paradigms for heating: alternating current heating (dissipation of magnetic waves, in the form of magnetohydrodynamic (MHD) waves, especially Alfvén waves); and direct current heating (dissipation of magnetic stress), usually by some form of magnetic reconnection, *e.g.*, nanoflares (see Klimchuk 2006 [40] for more details concerning AC and DC heating mechanisms).

Proposed alternating current heating mechanisms involve the dissipation of waves in the chromosphere and corona. Acoustic (Schwarzschild 1948 [60]), gravitational (Whitaker 1963 [75]), and MHD (Alfvén 1947 [3]) waves generated in the convection zone of the sun (beneath the photosphere) have been thought to propagate upwards into the atmosphere where they then dissipate their energy and heat the gas. How-

ever, Bruner (1980 [15]) found the acoustic wave energy flux to be three orders of magnitude too low to be considered a viable heating mechanism for the corona (which needs about 10^7 erg cm^{-2} s^{-1} in active regions). Excluding Alfvén waves, most waves likely dissipate below the corona and thus cannot be considered a viable heating mechanism (*e.g.*, Stein & Leibacher 1974 [62]). For example, in acoustic waves with small amplitudes, the crests of the waves travel faster than the leading edge, which creates large gradients in pressure and density, steepening into a shock that eventually leads to dissipation through viscosity or thermal conduction low in the solar atmosphere (Priest 1982 [54]). The resistance to dissipation of Alfvén waves in the lower atmosphere, however, is problematic because they are then also unlikely to dissipate in the corona (Parker 1988 [51]). Indeed, Alfvén waves have been observed in the solar wind propagating outwards from the sun (Velli & Pruneti 1997 [72] report the observations of Alfvén waves in the solar wind both in and out of the ecliptic plane, and always propagating away from the sun).

These shortcomings in the alternating current mechanisms led Parker to suggest another heating mechanism: nanoflares (Parker 1988 [51]). Lin *et al.* (1984 [42]) reported the observation of about 25 mi-

croflares (that is, solar flares with a power roughly 10^{-6} times the size of a typical solar flare) in the hard X-ray band (> 20 keV) with around 10^{27} erg s^{-1} of power in bursts lasting from a few to 20 seconds, which occurred at random intervals roughly 5 minutes apart. Moreover, the X-ray data had recurrent spikes during each event with durations of 1-2 s and energy around 10^{24} erg s^{-1} per spike (near the detection threshold of their balloon-borne X-ray detectors). These led Parker to hypothesize that what we observe as microflares are in fact superpositions of many nanoflares (10^{-9} times the power output of a typical solar flare). In other words, coronal loops may be heated intermittently with small bursts of energy, released through magnetic reconnection events. To date, no individual nanoflare has been directly observed. Moreover, direct observation is considered unlikely (Bradshaw & Cargill 2006 [12]; Reale & Orlando 2008 [56]; Bradshaw & Klimchuk 2011 [14]).

1.5 Magnetic Reconnection

Magnetic reconnection, a process found in nearly all magnetized plasmas throughout the universe, is "a topological restructuring of a magnetic field caused by a change in the connectivity of its field lines," (Priest & Forbes 2000 [55]). Figure 1-5 shows the general idea of re-

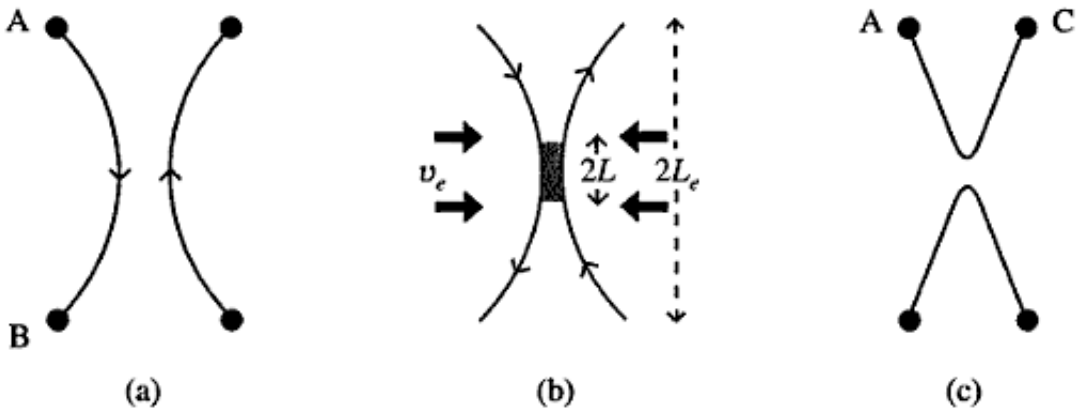

Figure 1-5: The basic scheme of magnetic reconnection. (a) Initially, oppositely-directed magnetic field lines that are independent of one another are somehow pushed together. (b) A short while later, a small diffusion region with a very strong magnetic gradient forms between the field lines. (c) The field lines break and reconnect with other lines into the lowest energy state, releasing excess energy as thermal and kinetic energy in the plasma. Taken from Priest & Forbes 2000 [55].

connection: a large spatial gradient formed between oppositely-directed field lines facilitates a breaking and reconnection of the field lines in a thin diffusion region that forms as the field lines come together (a small magnetic diffusivity coupled to a large gradient leads to diffusion and subsequent reconnection). The field reconfigures into a lower energy state, and excess magnetic energy is converted into thermal and kinetic energy of the plasma. Further, because the topology of the field has changed, particle trajectories and thermal conduction paths are also changed (Priest & Forbes 2000 [55]).

There are several different types of reconnection due to the complexities of the geometry and time evolution of the fields and contained

plasmas. The most basic type is known as Sweet-Parker reconnection (Sweet 1958 [63]; Parker 1958 [50]), whereby two opposing magnetic fields are simply pushed together and the size of the diffusion region L is roughly the length of the field line. Figure 1-6 shows an example of reconnecting field lines in the Sweet-Parker mechanism (from Parker 1958 [50]).

The rate at which the magnetic field lines enter the diffusion region in Sweet-Parker reconnection v_i is given by (Priest & Forbes 2000 [55]):

$$v_i = \frac{v_{Ai}}{R_{mi}^{1/2}} \tag{4}$$

$$v_A = \frac{B}{\sqrt{4\pi\rho}} \tag{5}$$

$$R_{mi} = \frac{L v_{Ae}}{\eta} \tag{6}$$

where the subscript i indicates inflows, the subscript e indicates external flow, v_A is the non-relativistic Alfvén speed, R_m is the magnetic Reynolds number, ρ is the mass density, and η is the magnetic diffusivity. In the Sweet-Parker mechanism, the length-scale of the system

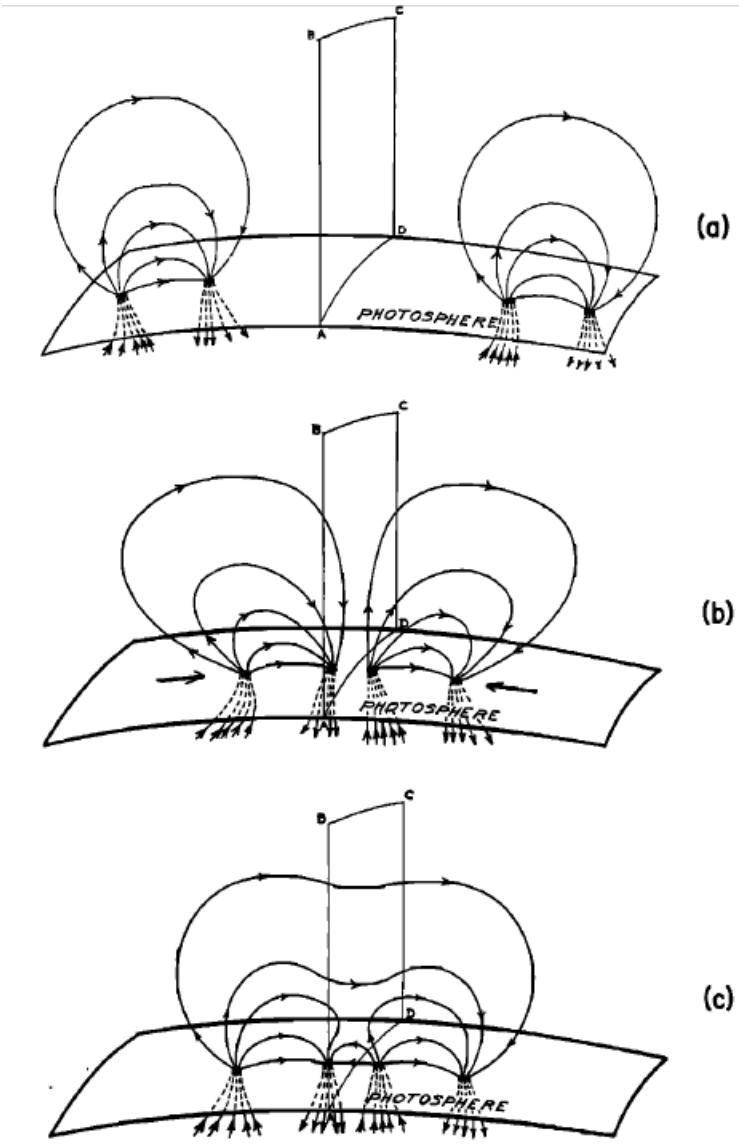

Figure 1-6: A schematic diagram of magnetic reconnection in two bipolar sunspots. Initially, the widely separated sunspots are forced together and, under the Sweet-Parker mechanism of reconnection, within a week the force lines reconnect. Taken from Parker 1958 [50].

tends to be extremely large, and thus the magnetic Reynolds number is large and the reconnection speed is rather small ($< v_A/1000$). In fact, this speed is far too slow to explain phenomena such as solar flares, which occur on an extremely fast time-scale with a large energy release.

A few years after the theory of Sweet-Parker reconnection was developed, Petschek (1964 [52]) suggested an alternative form of reconnection that could occur much more rapidly. He took the basic model of Sweet-Parker reconnection but changed a couple of features. First, the size of the diffusion region was reduced from essentially the entire field line to a much smaller segment, and since reconnection then occurs on a much smaller segment of the field lines, it can proceed much more quickly. Second, he argued that the Sweet-Parker mechanism ignored an important mechanism for the annihilation of magnetic energy: annihilation by propagation of Alfvén waves. He noted that if the magnetic field lines in the diffusion region were not perfectly antiparallel (that is, they possessed a component normal to the boundary), then Alfvén waves would propagate outwards. Between successive waves, the magnetic energy is reduced and converted into heat and kinetic energy in the plasma. The rate of this mechanism is independent of the plasma

conductivity, whereas the Sweet-Parker diffusion depends inversely on conductivity, so that the wave propagation mechanism becomes dominant at high plasma conductivities. These two factors placed the annihilation time of the field lines to within 100 seconds, well within the bounds of solar flares.

Petschek reconnection was accepted for many years as the driving mechanism behind solar flares, although there have been several alternate mechanisms proposed. Some (Sonnerup 1970 [61]; Yeh & Axford 1970 [81]) proved unsatisfactory, whether physically, mathematically, or both. However, there have been a large number of more recent improvements and subtleties added to treatments of reconnection that have yielded new insights and understanding: solving the problem in three dimensions (see Priest & Forbes [55]); solving the problem using a two-fluid plasma (*e.g.*, Cassak *et al.* 2005 [16]); investigating kinetic aspects of reconnection (Yamada *et al.* 2000 [79]); and more. The study of magnetic reconnection is still an active field of research in observing, experimental, and theoretical communities (see Yamada *et al.* 2010 for an excellent review of our current knowledge).

1.6 Radiation from Coronal Loops

Coronal loops are primarily observed in the extreme ultraviolet (EUV) and X-ray wavebands, to which the corona is optically thin. The energy loss per unit volume per unit time due to radiation from the corona, as a function of temperature, can be expressed as:

$$E_R = n^2 \Lambda(T) \tag{7}$$

where n is the number density (we presume charge neutrality, such that $n_e = n_i$; if that were not the case, an induced electric field would act to quickly restore charge neutrality) and $\Lambda(T)$ is called the radiative loss function. The radiative loss function is, in general, a complicated function of temperature (and to a lesser extent density). However, following Rosner, Tucker, & Vaiana (1978 [58]), it can be expressed as a piece-wise power law to a reasonable approximation:

$$\Lambda(T) = \chi T^{\alpha} \tag{8}$$

where the constants χ and α take different values in different temperature regimes. Because the radiative losses depend on the density

squared, and because the coronal density is many orders of magnitude lower than the photospheric density, then, at most wavelengths, emission from the optically-thick photosphere dominates. However, the photosphere is too cool to emit much in the EUV and X-ray bands, where the corona emits most strongly. Thus, in most cases, we observe the corona in high energy EUV and X-ray spectral lines. We can write the observed intensity (erg s^{-1} cm^{-2} sr^{-1}) of a given spectral line as (following Vaiana *et al.* 1973 [70]):

$$I(\lambda) = \frac{A}{4\pi f^2} \int n^2 ds \int_{\lambda_1}^{\lambda_2} p[\lambda, T(s)] \eta_{filter}(\lambda) d\lambda \tag{9}$$

where A is the surface area of the detector, f is the focal length of the telescope, s is the line-of-sight distance, $p(\lambda, T)$ is the power emitted at a given temperature and wavelength, η_{filter} is the filter transmission and telescope reflectivity at a given wavelength, and λ is the wavelength (λ_1 and λ_2 are the wavelengths at which η effectively drops to 0). η_{filter} is calculated in the laboratory for any instrument. We call the second integral in equation 9 the contribution function, $G(\lambda, T)$. The contribution function is calculated from databases of spectral line emission (see for example, Tucker & Koren 1971 [68] [69]; modern calculations make use of atomic databases like CHIANTI, Dere *et al.* 1997 [18];

Landi *et al.* 2012 [41] for the newly-released version 7).

In the present work, we will make substantial use of a quantity called the emission measure defined as:

$$EM(T) \equiv \int n^2 dV \tag{10}$$

where V is the volume of the emitting plasma. The emission measure may be interpreted as a measure of how much plasma is emitting radiation at a given temperature along the line-of-sight. For our purposes, it will be more convenient to make use of the so-called column emission measure, defined similarly:

$$EM_C(T) \equiv \int n^2 ds \tag{11}$$

where s is the distance along the line-of-sight. Note that since the corona is optically thin, the line-of-sight may include many superimposed, but spatially separated, sources of emission. The intensity of a spectral line is a function of the column emission measure:

$$I(\lambda) = \frac{A}{4\pi f^2}\, EM_C(T)\, G(\lambda, T) \tag{12}$$

If we can reasonably sure that two spectral lines are being emitted from the same volume of plasma, then we can use the ratio of their intensities to approximate the plasma temperature, because their ratio will only be dependent upon the known contribution functions. Further, given the intensity of a spectral line and the contribution function at its formation temperature, we can then determine the column emission measure (the method of emission measure loci, see Jordan *et al.* 1987 [37]). Finding the column emission measure in this way using spectral lines formed at a range of temperatures then tells us whether the plasma is isothermal, or, if it is multithermal, how multithermal it is. Note that these techniques only work for plasmas in thermal equilibrium.

For some spectral lines, the intensity of emission does not depend on n^2, but rather n^β where $\beta \neq 2$ (for example, lines emitted from electrons excited to metastable levels). Through prudent choices of lines, a ratio of intensities can be used to give an estimate of the electron density (let's call the density estimated this way n_{Ratio}). Further, if we approximate the emission measure by n^2V with an estimate of the resolved volume V_{EM}, we can then find another density estimate (n_{EM}). Determine the emission measure observationally, and then the filling factor (as defined in equation 3) can be found:

$$EM = n_{EM}^2 V_{EM} \tag{13}$$

$$n_{EM}^2 = EM/V_{EM} \tag{14}$$

$$f = \frac{V_{Ratio}}{V_{EM}} = \frac{EM/n_{Ratio}^2}{EM/n_{EM}^2} = \frac{n_{EM}^2}{n_{Ratio}^2} \tag{15}$$

Recall that a filling factor less than 1 implies that unresolved filamentary structures comprise the coronal loop. Thus, determining the emission measure, calculating the density of the emitting plasma, and estimating the resolved volume, allows us to determine whether we have resolved the basic structure of the corona.

1.7 Emission Measures of Active Region Loops

In recent years, it has become clear that there exist significant discrepancies between observationally measured emission measures of active region coronal loops and those calculated using numerical models. In a recent paper, Warren *et al.* (2011 [74]) performed observations using two instruments aboard the Japanese satellite Hinode, the Extreme-Ultraviolet Imaging Spectrometer (EIS) and the X-Ray Telescope (XRT), and then ran two numerical simulations of loops heated with high- and low-frequency bursts of energy. Figure 1-7 shows the

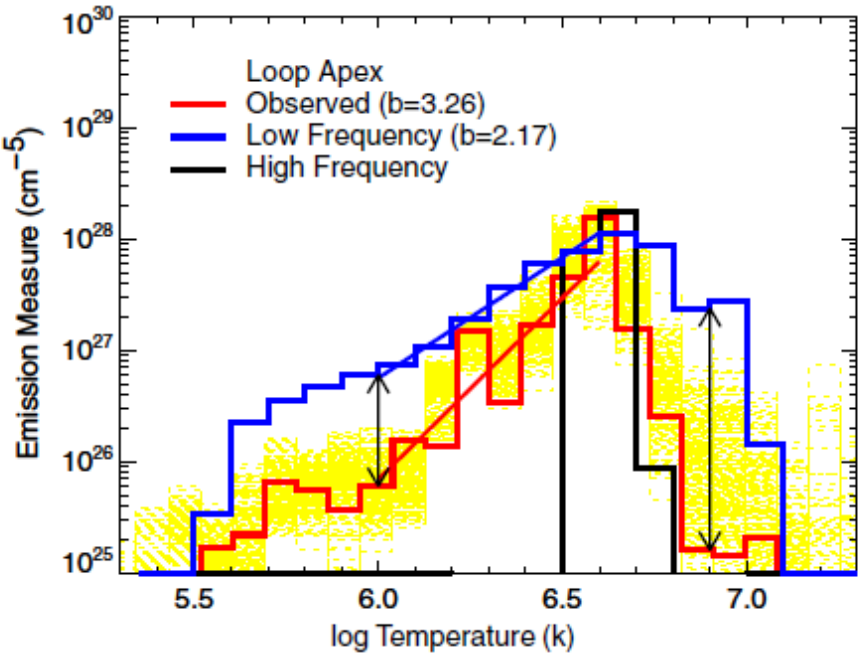

Figure 1-7: Column emission measures found at the apex of a coronal loop in an active region. The red line shows the result found observationally with Hinode's EIS and XRT instruments, and the yellow indicates error bars on the calculations (performed with a Monte Carlo Markov Chain algorithm). The blue line is the theoretically obtained emission measure given low frequency heating events; the black line is that obtained for high frequency heating events. Taken from Warren *et al.* 2011 [74]

column emission measure as a function of temperature found for each case. If we claim that the emission measure from its peak of emission down to about 1 MK can be written as a power law (EM $\sim T^b$) for some index b, then we can easily compare the results of observations with theoretical values (see Jordan 1975 [35]; Jordan 1980 [36]).

For the observed case, Warren *et al.* found that the EM peaks around $10^{6.6}$ K, with a power-law index of 3.26 down to 1 MK, and an even sharper drop-off of higher temperature plasma. In other words, in

an active region core, the plasma is mostly concentrated around $10^{6.6}$ K, with very little plasma above that temperature, but some non-negligible amount at lower temperatures.

In the high-frequency heating simulation, the loops were heated with bursts of energy of 9.28×10^{-2} erg cm^{-3} s^{-1} for durations of 13 s, at intervals of 150 s (very little time to cool significantly in between events). As a result of the short duration between heating events, the bundle is composed of loops all at nearly the same temperature. Hence, the EM calculated in this case is essentially isothermal, peaking around $10^{6.7}$ K, and dropping extremely rapidly at lower and higher temperatures.

In the low-frequency heating simulation, the loops were heated with bursts of energy of 2.22×10^{-1} erg cm^{-3} s^{-1} for durations of 67 s, at intervals of 1800 s (ample time to cool significantly in between heating events). The apex temperature after each heating event reached slightly over 10 MK and falls to nearly 0.4 MK, maintaining its temperature around a few MK for a long period of time (as the density nears its maximum, see figure 6 of Warren *et al.*). The EM found for this case thus shows a peak of around $10^{6.6}$ K, with an abundance of plasma at higher temperatures slightly over 10 MK and an abundance at lower

temperatures (and therefore a shallow power-law index of 2.17).

Therefore, Warren *et al.* have found significant discrepancies between the numerical models and observations. On the one hand, the high-frequency simulation significantly underestimates the amount of plasma at lower temperatures, while the low-frequency simulation predicts an over-abundance of plasma at temperatures both higher and lower than the peak of the EM. Warren *et al.*, in the discussion section of their paper, note that they have tried a simulation of more intermediate frequency, which more closely matches the EM, but that they cannot consistently predict intensities of some of the spectral lines.

Other recent papers (*e.g.*, Winebarger *et al.* 2011 [78]; Tripathi *et al.* 2011 [67]) have found similar results. In all cases, the observed power law index b is greater than can be found from numerical models. In the present work, we wish to address the causes of these discrepancies, and, in doing so, shed light on the heating mechanisms of active region coronal loops.

2 Numerical Modeling

2.1 Hydrodynamics in Low-β Plasma

The current work presents the results of numerical calculations performed to investigate the time-dependence of heating mechanisms of coronal loops. The calculations were carried out using the HYDRAD code (Bradshaw & Mason 2003a,b [9] [10]; Bradshaw & Klimchuk 2011 [14]; *etc.*), which solves the one-dimensional hydrodynamics equations appropriate to describing the behavior of a two-fluid plasma confined to an isolated magnetic strand. Under the assumptions of quasi-neutrality ($n_e = n_i$) and current-free conditions ($v_e = v_i$), the hydrodynamics equations are as follows:

(i) Conservation of mass

$$\frac{\partial \rho}{\partial t} = -\frac{\partial (\rho v)}{\partial s} \tag{16}$$

where ρ is the mass density ($\approx n m_i$), t is the time, v is the bulk-flow velocity, and s is the field-aligned spatial coordinate.

(ii) Conservation of momentum

$$\frac{\partial(\rho v)}{\partial t} = -\frac{\partial(\rho v^2)}{\partial s} - \frac{\partial(p_e + p_i)}{\partial s} + \frac{\partial}{\partial s}(\frac{4}{3}\mu_i \frac{\partial v}{\partial s}) + \rho g_{\parallel} \qquad (17)$$

where $p_e = nk_BT_e$ and $p_i = nk_BT_i$ are the electron and ion pressures, respectively, μ_i is the coefficient of viscosity for the ions (and we neglect that of the electrons as $\frac{\mu_e}{\mu_i} \propto (\frac{m_e}{m_i})^{1/2}(\frac{T_e}{T_i})^{5/2}$ will be small except when the electron temperature is extremely high compared to the ion temperature), and $g_{\parallel}$ is the field-aligned gravitational acceleration.

(iii) Conservation of energy

Electrons:

$$E_e = \frac{1}{\gamma - 1} p_e \qquad (18)$$

$$\begin{aligned} \frac{\partial E_e}{\partial t} &= -\frac{\partial}{\partial s}[(E_e + p_e)v] + v\frac{\partial p_e}{\partial s} + \frac{\partial}{\partial s}(\kappa_{e0} T_e^{5/2} \frac{\partial T_e}{\partial s}) \\ &\quad + \frac{1}{\gamma - 1} k_B n \nu_{ei}(T_i - T_e) - E_R + E_H \end{aligned} \qquad (19)$$

where E_e is the electrons' internal energy density, κ_{e0} is the coefficient of electron thermal conductivity, T_e and T_i are the electron and ion temperatures, γ is the adiabatic index, and ν_{ei} is the electron-ion collision frequency, E_R is the energy lost by radiation per unit volume, and

$E_H(s,t)$ is the energy input per unit volume by heating as a function of position and time. The terms on the right-hand side of equation 19 represent the input, removal, and redistribution of electron energy by various mechanisms. The first term is the transport of energy along the coronal loop through a bulk flow (a change of enthalpy flux with position). The second term represents the work done by the small electric field induced from a small charge imbalance ($eE = -\frac{1}{n}\frac{\partial p_e}{\partial s}$). The third term represents the transport of energy through thermal conduction. The fourth term is the exchange of energy between the electrons and ions due to inter-species collisions. The fifth term is the energy lost through radiation (line emission and *bremsstrahlung*). Finally, the last term is the energy input into the coronal loop through some heating mechanism (see next section for more details).

Ions:

$$E_i = \frac{1}{\gamma - 1} p_i + \frac{1}{2}\rho v^2 \tag{20}$$

$$\begin{aligned} \frac{\partial E_i}{\partial t} &= -\frac{\partial}{\partial s}[(E_i + p_i)v] - v\frac{\partial p_e}{\partial s} + \frac{\partial}{\partial s}(\kappa_{i0} T_i^{5/2}\frac{\partial T_i}{\partial s}) \\ &\quad + \frac{1}{\gamma - 1} k_B n \nu_{ei}(T_e - T_i) + \frac{\partial}{\partial s}(\frac{4}{3}\mu_i v\frac{\partial v}{\partial s}) + \rho v g_{\parallel} \end{aligned} \tag{21}$$

where E_i is the ion energy density and κ_{i0} is the coefficient of ion thermal conductivity. The terms on the right-hand side of equation 21 similarly represent the input, removal, and distribution of ion energy. The first four terms are equivalent to those above. The fifth term represents the work done by viscous stress on the bulk flow, while the last term is the work done by gravity (note that this was neglected for the electrons because their mass density will be smaller by a factor of the mass ratio ≈ 1835).

To calculate the losses by radiation, HYDRAD makes use of the CHIANTI database (Dere *et al.* 1997 [18]) along with the following equations:

$$E_R(X) = n^2(0.83 \times Ab(X) \times \sum_{i=1}^{i=Z+1} \epsilon_i X_i) \tag{22}$$

$$\frac{\partial X_i}{\partial t} = -\frac{\partial (X_i v)}{\partial s} + n(I_{i-1}X_{i-1} + R_i X_{i+1} - I_i X_i - R_{i-1}X_i) \tag{23}$$

where X denotes a given element (and we need to sum the contributions from the most abundant coronal elements: H, He, C, N, O, Ne, Na, Mg, Al, Si, S, Ar, Ca, Fe, Ni), 0.83 is the proton-to-electron ratio in

the corona, $Ab(X)$ is the coronal abundance of element X relative to hydrogen, Z is the atomic number, ϵ_i is the emissivity of all lines from charge state i of element X (where $i = 1$ is neutral) as calculated from CHIANTI, X_i is the population fraction of charge state i, I_i is the ionization rate of charge state i, and R_i is the recombination rate of charge state i. Note that HYDRAD can also use a piece-wise power law fit (equation 8) to the radiative losses if desired (to save calculation time).

Before we specify heating events to study the subsequent evolution of the coronal loop, we must determine an initial loop profile (temperature, density, and velocity along the loop) to use with HYDRAD. We specify the loop geometry: total length, foot-point height, and inclination from the vertical direction (generally assuming semi-circular, although HYDRAD can handle arbitrary geometry through specification of $g_{\parallel}(s)$). We also specify the foot-point density and temperature. Then, the equations of energy and pressure are integrated from foot-point to foot-point to determine the pressure and temperature as functions of position throughout the whole loop. At both the foot-points and apex, it is assumed that the conductive flux is zero. From these two values, we can then determine the density as a function

of position, and it is assumed that the bulk-flow velocity is initially zero everywhere (hydrostatic equilibrium). Using the hydrodynamic equations and the initial loop profile, we can then specify some heating event(s) $E_H(s,t)$, that perturbs the energy balance, and follow the subsequent loop evolution.

2.2 Heating

After determining the initial loop profile, we then would like to investigate possible heating mechanisms by choosing an appropriate form of $E_H(s,t)$, solving the hydrodynamic equations to evolve the loop in time, and then comparing the resulting emission structure against observations. For example, if we wish to model impulsive heating by nanoflares, then we need to determine a suitable functional form of $E_H(s,t)$ that approximates the spatial and temporal properties of the energy input predicted by Parker (1988 [51]).

From observations, we expect the emission measure to peak around 4-5 MK (*e.g.*, Warren *et al.* 2011 [74]), and so the volumetric heating rate must be strong enough to heat the loop to at least these temperatures (or higher), such that the emission measure peaks in this range. We can determine an approximate volumetric heating rate as follows

(assuming that we heat the electrons preferentially, see below).

At the onset of heating, we expect that the loop will be tenuous ($n \approx 10^8$ cm^{-3}), and thus very quickly heated ($T_e \approx 5$ MK). We find the timescales for energy changes due to radiation (τ_R) and thermal conduction (τ_{Con}), to show that early on conduction drives the temperature change:

(1) Energy change due to radiation alone:

$$\frac{\partial E}{\partial t} = -E_R = -n^2 \chi T^{\alpha} \tag{24}$$

To order of magnitude, this becomes:

$$\frac{3 k_B n T}{\tau_R} \approx n^2 \chi T^{\alpha} \tag{25}$$

where χ and α are the constants of the piece-wise power law fit to the radiative loss function. Thus,

$$\tau_R \approx \frac{3 k_B T^{1-\alpha}}{n \chi} \approx 2 \times 10^5 \text{ s} \tag{26}$$

for $n \approx 10^8$ cm^{-3}, $T_e \approx 5$ MK, $\alpha = -1/2$, and $\chi = 10^{-18.66}$.

(2) Energy change due to thermal conduction alone:

$$\frac{\partial E}{\partial t} = -\frac{\partial F_C}{\partial s} \tag{27}$$

where $F_C = -\kappa_0 T^{5/2} \frac{\partial T}{\partial s}$ is the Spitzer formula for thermal conduction. To order of magnitude, we have:

$$\frac{3k_B nT}{\tau_{Con}} \approx \frac{1}{L_T}(\kappa_0 T^{5/2} \frac{T}{L_T}) \tag{28}$$

where L_T is a characteristic coronal length scale. So,

$$\tau_{Con} \approx \frac{3k_B n L_T^2}{\kappa_0 T^{5/2}} \approx 12 \text{ s} \tag{29}$$

for $n \approx 10^8$ cm^{-3}, $T_e \approx 5$ MK, and $L_T \approx 4 \times 10^9$ cm.

Thus, we can see that thermal conduction dominates any temperature changes in the corona shortly after the onset of heating for the parameters considered. As the loop gradually fills, the relative importance of radiation increases (and the plasma also requires more energy for such drastic changes in temperature). We can then calculate the approximate volumetric heating rate to attain a given maximum temperature as follows. Consider a simplified energy equation, where only the heating and thermal conduction terms are considered (the dominant terms early on):

$$\frac{\partial E}{\partial t} = 3k_B n \frac{\partial T}{\partial t} = E_H - \frac{\partial F_C}{\partial s} \tag{30}$$

The plasma reaches its maximum temperature when $\frac{\partial T}{\partial t} = 0$, so:

$$E_H = \frac{\partial F_C}{\partial s} \approx \frac{\kappa_0 T_{max}^{7/2}}{L_T^2} \tag{31}$$

For constant heating reaching a maximum temperature of around 5 MK, we find $E_H \approx 0.02$ erg cm^{-3} s^{-1}.

There is one slight concern with the above derivation: Spitzer's formula for thermal conduction only holds for sufficiently low mean-free paths (we follow Bradshaw & Cargill 2006 [12]). In other words, there is a limit to how much thermal flux a given density of particles can transport. In this case, the thermal flux is given by:

$$F_C = E_{Th} v_{Th} = \frac{3}{2} n k_B T \times \sqrt{\frac{3 k_B T}{m}} = \frac{n (3 k_B T)^{3/2}}{2\sqrt{m}} \tag{32}$$

Equating this equation with the Spitzer formula, we can determine the temperature above which the flux will be saturated:

$$T_{crit} = (3 k_B)^{3/4} (\frac{n L_T}{2 \kappa_0 \sqrt{m}})^{1/2} \tag{33}$$

For electrons, with the above parameters, we obtain a critical temperature of around 7.5 MK (about 1.1 MK for protons). Thus, we expect

to reach this regime briefly during the initial heating of a loop, which HYDRAD does take into account.

In the current work, we preferentially heat the electrons instead of the ions, although it is unknown whether that is physically correct. There are two problems with determining which species (or both) is heated. First, there is no straightforward way to determine the ion temperature (unlike the electron temperature which can be determined from spectral lines). Second, since coronal loops radiate most strongly when they are denser (equation 7), and since the inter-species collision frequency increases with density (equation 34), by the time we observe most loops the two species will have thermally equilibrated. Since they have equilibrated when we observe them, indications of which species was heated are lost.

2.3 Common Assumptions

To elucidate the physics behind the equations, the assumptions that go into the current modeling, as well as their justifications, are now specified and discussed. It is the author's hope that it will also give some insight into the physical processes occurring in the coronal loops we study.

(1) We perform calculations in one spatial dimension (s, along the coronal loop).

To justify this assumption, we first note that at coronal temperatures ($> 10^6$ K), its constituent atoms will be ionized (not necessarily fully ionized though). For example, in the corona, at temperatures above $10^{4.6}$ K, hydrogen will be fully ionized, while helium atoms will have lost both electrons at temperatures above $10^{5.2}$ K, while iron retains over half of its electrons at 10^6 K (see Mazzotta *et al.* 1998 [47]). Thus, the particles will be constrained to follow the magnetic field lines, according to the Lorentz force law. Further, since the corona has a low plasma β value, the magnetic field confines the plasma in narrow flux tubes, and there will be little cross-field transport. Further, the thermal conductivity parallel to the magnetic field far exceeds the conductivity perpendicular to the field (Goedbloed & Poedts 2004 [28]). Thus, for our purposes, it will suffice to consider the particles as constrained to travel in one dimension, along the coronal loop.

(2) The loop is semi-circular in geometry and line-tied at each footpoint.

As noted in the introduction, observationally, coronal loops are observed to be nearly semi-circular, although they can be slanted towards

one of the footpoints if the magnetic field is stronger on one side(as found in Berton & Sakurai 1985 [6]). It has been known for many years that coronal loops are anchored magnetically in the photosphere (see, for example, van SpeyBroeck *et al.* 1970 [71]). As shown in figure 1-3, the plasma β in the photosphere is greater than 1, and so the plasma there will not be constrained by the magnetic field as strongly as in the corona, and so the foot-points will be subjected to convective motions, which twist the field lines and drive magnetic reconnection. In the corona, due to the high degree of ionization, the electrical conductivity, and thus the magnetic Reynolds number (equation 6), is large. Alfvén (1943 [2]) showed that in plasmas with a large magnetic Reynolds number, the field lines are essentially frozen into the plasma (the field lines are dragged by the plasma or they push the plasma, but the two always move together). This frozen-in flux theorem implies that loops in the corona will be anchored in the photosphere.

(3) The heating is spatially uniform along the coronal loop.

For nanoflare heating, or in full-sized solar flares, the heating is not spatially uniform. However, in the corona, the thermal conduction is extremely large (in the energy equations, the term $\frac{\partial}{\partial s}(\kappa_0 T^{5/2}\frac{\partial T}{\partial s})$ represents the redistribution of energy by thermal conduction). Because

this term has a strong dependence on the temperature, and because the temperature along coronal loops is extremely high with low density, the thermal conduction acts very quickly and efficiently to redistribute the heat input throughout the coronal loops.

If we perform a rough calculation of the time-scale in which conduction acts immediately after a loop is heated, we can show this readily (we use equation 29 once again). For the first few seconds of heating, the loop is relatively tenuous and thus the temperature increases rapidly (lots of energy per particle). Taking $n \approx 10^8$ cm^{-3}, $T \approx 5 \times 10^6$ K, and $L_T \approx 4 \times 10^9$ cm, we found the conduction time-scale to be about 12 seconds. Thus, for heating events lasting around a minute or more, thermal conduction will act to distribute the energy so that the heating will look essentially uniform.

Winebarger & Warren (2004 [76]) ran a few numerical simulations to determine what effects would arise for heating events with different locations, length scales, and heating rate, but all with the same total energy input. They conclude that once the conductive and radiative cooling timescales become roughly equivalent (after initial heating), all of the loops evolve in the same way with roughly the same apex densities and temperatures. Observationally (since we only ever observe loops in

cooling phases), this implies that we could not distinguish loops that were heated uniformly from loops that were heated in much smaller volumes. In other words, thermal conduction is an irreversible process; once it has diffused the energy across the loop, the initial temperature profile cannot be recovered.

(4) The plasma is a two-species fluid (ions and electrons).

If the heating were on time-scales much longer than the inter-species collisional time-scale, then the inter-species collisions would act to thermally equilibrate the species fast enough that their temperatures would remain equal to each other, and we could then use single-fluid equations. Let us perform a rudimentary calculation to show that this may not be the case. The collision frequency ν_{ei} is given by:

$$\nu_{ei} = \frac{\sqrt{32\pi} q_e^2 q_i^2}{3 m_e m_i} n \left(\frac{k_B T_e}{m_e}\right)^{-3/2} \ln \Lambda \tag{34}$$

where q_e and q_i are the electron and ion charges, m_e and m_i are the electron and ion masses, and $\ln \Lambda$ is the Coulomb logarithm ($\approx$ 20 in the corona). If we take the density to be $\approx 10^8$ cm^{-3} and the electron temperature to be $\approx 5 \times 10^6$ K, we find a collisional timescale ($\approx 1/\nu_{ei}$) of about 45 minutes. We expect the heating to occur on much

smaller timescales (judging from observable solar activity), and thus we conclude that a single-fluid treatment does not suffice for studies of impulsive heating.

(5) The radiative loss function can be approximated by a piece-wise power-law function.

As noted by Rosner, Tucker, & Vaiana (1978 [58]), the calculation of the radiative loss function (equations 22 & 23) is dependent upon the accuracy of the atomic physics (*i.e.*, values obtained from the atomic databases like CHIANTI) and the coronal abundances of the elements. Unfortunately, both of these carry an amount of uncertainty with them, and slightly different values can lead to radically different radiative loss functions. However, if we do not need to know the precise details of the functional form of $\Lambda(T)$, then we can approximate the loss function by a piece-wise power-law given that our approximation is within the uncertainties of a full, detailed calculation. The values specified by Rosner, Tucker, & Vaiana are outdated, but the concept remains correct, and the calculations are significantly quicker using this approximation. Our results from chapter 3 use the full calculation of the radiative loss function, while those in chapter 4 use this approximation.

2.4 Emission Measure Calculations

In our model, we calculate the emission measure in two different ways. (1) We calculate a true emission measure that has no dependence on instrumental or line-of-sight constraints (*i.e.*, what would be seen with a perfect detector looking at active region loops). We can do so because we have access to the values of density and temperature produced by our model, a luxury not available to observers. (2) We calculate a synthetic observed emission measure along the line-of-sight that an instrument (*e.g.*, Hinode-EIS) would see if it were to observe loops in an active region identical to our model loops. By calculating the two emission measures, we can see what features of the true emission measure are reliably reproduced in the observed one and what information about the state of the plasma is lost. We can then be confident in the information that we extract in the real, observed emission measure.

To begin, we calculate the real emission measure. Recall that the column emission measure is defined as

$$EM_C = \int n^2 dr \tag{35}$$

where dr is along the line-of-sight. We assume that we observe a single, isolated coronal loop. We model its emission measure as if the loop were composed of a bundle of isolated, sub-resolution strands in various stages of heating and cooling. With HYDRAD, as our loop evolves, the code will output a profile of the density, temperature, and velocity as a function of position at a given time interval (which we take every second).

A real coronal loop that is multithermal would be composed of many different strands in various stages of heating and cooling (recall that observed loops have filling factors much less than one). The majority of strands at any given time will be cooling, with a few being actively heated, and the cooling strands will contribute the most to the emission measure for the following reason. At the onset of heating in a given strand, the density will be low, and the temperature will rise rapidly. The initial energy transport will be due primarily to thermal conduction (as explained before), and so the energy will flow down towards the chromosphere. The chromosphere will be unable to radiate all of the excess energy being delivered to it, and so the pressure will increase and the chromosphere will expand upwards, causing a flow of material into the corona. Thus, after a heating event, the density of

the corona will increase, and it will radiate more strongly ($E_R \propto n^2$). The highest density will be achieved after heating ceases, so the strands that are cooling will contribute the most to an emission measure.

We similarly construct a monolithic coronal loop composed of many different strands in various stages of heating and cooling in our model. Rather than run thousands of different simulations for each strand, we choose to treat each snapshot in time of one simulation as a strand that composes a single monolithic structure. The majority of strands will be in cooling phases, with a few being actively heated. The emission measure will be dominated by the cooling strands, for the same reason as above. In this way, the various phases of loop evolution that exist in active region loops will be accounted for when calculating the emission measure.

We first calculate the emission measure near the loop apex for a single strand, taking advantage of the fact that we have the numerical values of the density and temperature at every position. Because the grid cell width ds is perpendicular to the line-of-sight, we need to convert to a line-of-sight measurement. It should also be noted that the size of a grid cell ds is not constant over the loop (*i.e.*, HYDRAD uses adaptive grid cell binning). To start, we find the mean of the

density-squared near the loop apex:

$$< n^2 >= \frac{\int n^2 ds}{\int ds} = \frac{\int n^2 ds}{S} \tag{36}$$

where $S = \int ds$ is the length of the section over which we find the average. Now, if we imagine looking down at the loop from above, the emission measure for this single strand would be given by the mean density-squared times the line-of-sight depth divided by the number of strands N (since the line-of-sight contains N strands in a small volume). Taking the line-of-sight depth to be about one arc-second (corresponding to about 725 km on the sun or the size of a pixel for Hinode-EIS), we have for a single strand:

$$EM_C \approx < n^2 > \times \frac{1 \text{ arcsec}}{N} \tag{37}$$

We can easily scale this by choosing different line-of-sight depths. For the entire coronal loop, we then sum over all the strands to find our total emission measure:

$$EM_C = \sum(< n^2 > \times \frac{1 \text{ arcsec}}{N}) = \sum(\frac{\int n^2 ds}{\int ds} \times \frac{1 \text{ arcsec}}{N}) \tag{38}$$

In effect, we have found an average of the emission measure in the corona. This emission measure is free of observational concerns such as instrument response, and is thus a real emission measure.

However, in order to make predictions and comparisons with an observationally determined emission measure, this approach does not suffice. We must account for instrumental, observational, and line-of-sight issues. The photon flux at a particular wavelength detected by a satellite depends on a number of parameters: its distance from the source, instrument response (plate scale, quantum efficiency, gain, pulse pile-up), area of the detector, number of pixels, spatial and spectral resolution, cadence, and the satellite's orbital parameters.

Conceptually, the way we synthesize an observed flux is explained well by Bradshaw & Klimchuk (2011 [14]; also see figure 2-1). We create a virtual instrument, modeled after a real one such as Hinode-EIS, where we know the spatial, spectral, and temporal resolution for a given wavelength and a response function that essentially converts an incident photon flux into measured quantities reported in instrumental units (for example, converting photons s^{-1} cm^{-2} sr^{-1} to DN $pixel^{-1}$ s^{-1}). We assume that the photons are emitted isotropically and that from each small section of a coronal loop a certain number of photons

are detected by a given pixel. Since we have the loop profiles (density, temperature, flow speeds, and ion populations) at a given position, with the aid of an atomic database, we can calculate which spectral lines will be emitting with what intensity at a given position in a loop. We calculate the detected intensity of each line seen by a pixel with the aid of an equation like equation 9, which takes into account the instrument response. For imaging instruments (such as SDO-AIA), we then sum up the emission from all of the lines from each of the loops detected within a pixel, and thus build up a synthesized flux. For spectrometers (such as Hinode-EIS), we record the intensity of individual lines to build up a synthesized spectrum.

We do exactly with our synthesized fluxes as an observer would with a real, observed flux to build up an emission measure with which we can make direct comparisons. We make use of equation 12, which specifies the column emission measure in terms of line intensity, contribution function, and the area and focal length of the detector. We have calculated the intensity of lines detected by our virtual instrument, we know the satellite parameters, and we can use an atomic database to determine the contribution function for a given line. We therefore use a number of strongly emitting lines formed across a range of tempera-

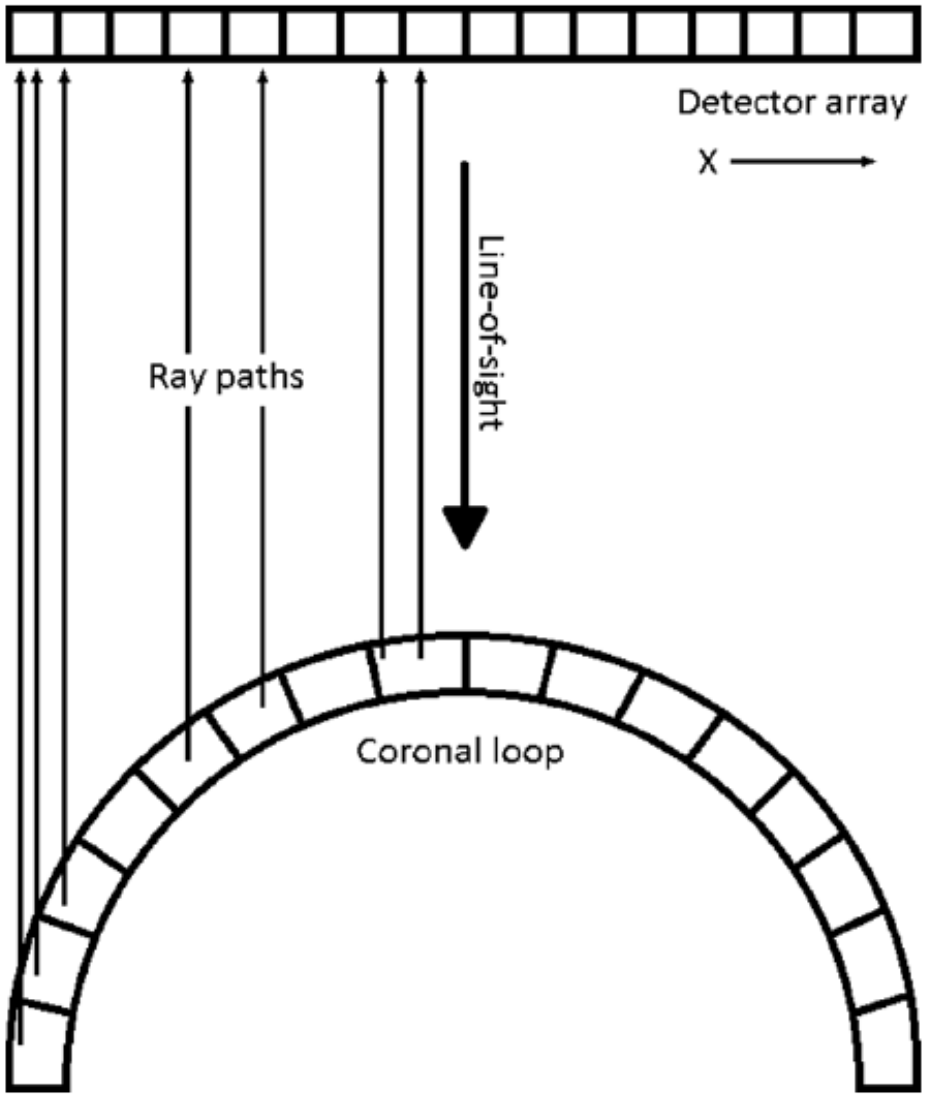

Figure 2-1: A visualization of the method by which we synthesize a flux for a detector such as Hinode-EIS. The grid cells of width *ds* are projected onto the virtual detector. The intensity of each (accounted for) spectral line from each grid cell are then binned into the appropriate pixel. For an imager, the emission is summed from each grid cell and from each strand which comprises the total coronal loop. For a spectrometer, the intensity of the individual lines are recorded to create a spectrum. We then have a prediction of the emission for a coronal loop. Image taken from Bradshaw & Klimchuk (2011 [14]).

tures to calculate a so-called emission measure loci plot (Pottasch 1963 [53]; Jordan *et al.* 1987 [37]) for each pixel in our virtual detector.

This Pottasch method essentially stems from equation 12: we measure the intensities of various lines and compute the contribution functions for those lines, and thus can determine the emission measure. There is one slight subtlety to the method: Pottasch made the assumption that the radiation of a given line originates primarily where the contribution function is within a third of its maximum value. This corresponds to making the assumption of a constant contribution function:

$$< G(T) >= 0.7 \max(G(T)) \tag{39}$$

Pottasch checks this assumption near the end of his paper and notes that 87% of the radiation indeed originates there. The motivation behind this assumption was that the contribution function drops off very rapidly away from its maximum, and thus it would simplify calculations (we adopt this simplification and neglect the remaining 13%). See figure 2-2 for an example of an emission measure loci plot from a recent observational study (Tripathi *et al.* 2011 [67]).

With the Pottasch method, we then have an emission measure plot

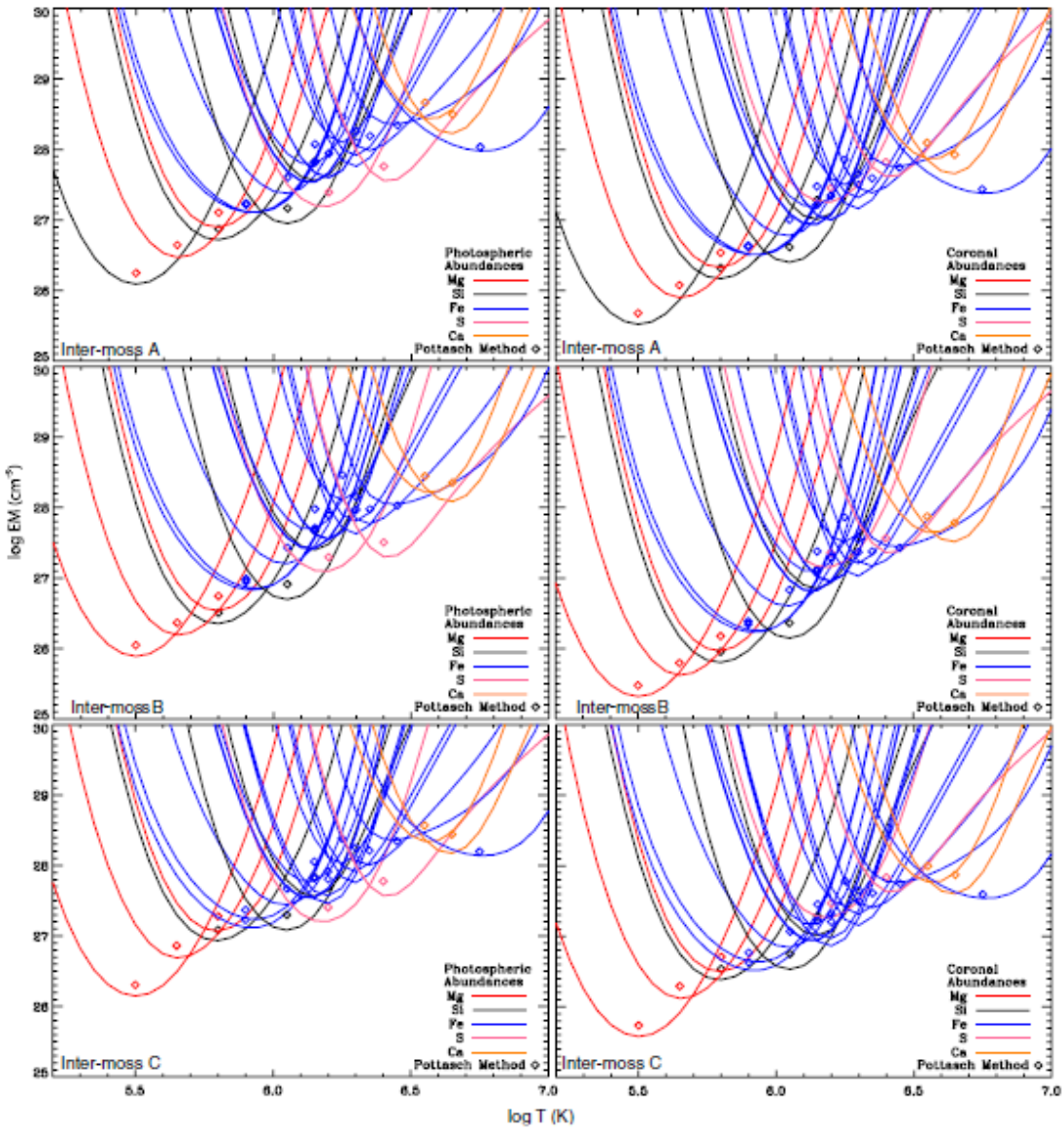

Figure 2-2: Example of an emission measure loci plot, taken from Tripathi *et al.* (2011 [67]). The six figures are emission measures of three moss regions within active regions (calculated using photospheric abundances on the left and coronal abundances on the right) determined observationally with a mixture of TRACE, Hinode-EIS, and Hinode-XRT. The inverted-U curves are the emission measure loci, while the diamonds mark values determined using the Pottasch method. In the current work, we will calculate emission measures in a similar manner.

that we can directly compare to observations to test our models. We use our model to compare both with the real emission measure considered before and with the emission measures that observers have previously calculated for active region loops. In this way, we hope to constrain the heating mechanisms occurring within active regions in the corona by linking properties of the heating (*e.g.*, its time dependence) directly to properties of the emission measure (*e.g.*, the power-law index between the peak and 1 MK). We aim to address the discrepancy in the power law index found by theorists and observers.

3 Heating by a single nanoflare storm

To begin our study of heating of coronal loops by nanoflares, we ran six simulations with HYDRAD for various durations of heating, for a single heating event. This heating event, which we term a nanoflare storm, is a continuous release of energy for a given duration of time consisting of a number of nanoflares in succession (not necessarily on the same magnetic strand), which eventually ceases and the loop is allowed to cool. If the magnetic field stores and releases energy, then there must be a limit to how long heating by magnetic reconnection can last. Compare the release of energy in solar flares (thought to be due to magnetic reconnection): typically their rise phase lasts for no more than ten minutes before the flaring loop begins to cool dramatically and high temperature emissions drop off. We choose heating events for our simulations consisting of energy release for up to a maximum of ten minutes.

The same initial loop profile was used in all the simulations. The total loop length, from foot-point base to foot-point base (where the base is at the solar surface), was 10^{10} cm (100 Mm), with isothermal chromospheres of 10^9 cm at each foot-point, thus leaving a coronal

length of 8×10^9 cm. The loop was not inclined from the vertical direction. The initial density and temperature profiles along the loop are shown in figure 3-1.

As explained in the Introduction, the loop length, inclination, and foot-point density and temperature were chosen (based on observational values). To then obtain the density and temperature as a function of position, the steady-state hydrodynamic equations were integrated along the loop (using a constant background heating). The initial bulk flow velocity was assumed to be zero everywhere. The resulting loop contains three distinct regions of the atmosphere: the chromospheric foot-point (at around 20,000 K), the transition region where the temperature rises and the density falls sharply, and the tenuous corona (review figure 1-2). The chromospheric base acts as a source and sink of mass and energy as the loop plasma evolves and acts a base for our computational domain (*i.e.*, we do not attempt to treat the lower atmosphere in more detail). We then input appropriate heating parameters to simulate the event we wish to study (for a coronal length scale of 4×10^9 cm from the apex to the top of the chromosphere and maximum temperature of around 10 MK, we find $E_H \approx 0.2$ erg cm^{-3} s^{-1} using equation 31).

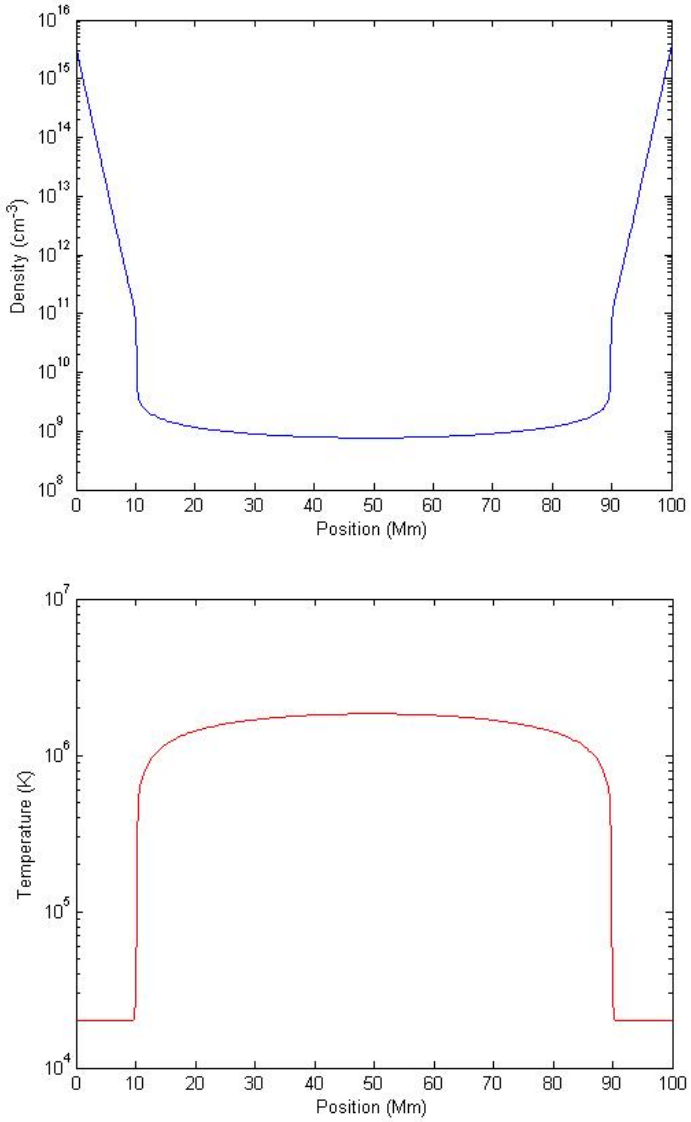

Figure 3-1: The initial density and temperature profiles as a function of position along the coronal loop. Each of the six simulations described in this section had the same initial profile. The ions and electrons were initially in thermal equilibrium. The first and last ten megameters of the loop are chromospheric foot-points, and the next megameter or two is the sharp transition region, leading into the corona. See figure 1-2 to review the layers of the atmosphere.

The radiative losses were treated with a full calculation (*i.e.*, not the power-law approximation); fifteen elements were accounted for (H, He, C, N, O, Ne, Na, Mg, Al, Si, S, Ar, Ca, Fe, Ni), of which fourteen were treated with ionization equilibrium calculations and one (Fe) was done with non-equilibrium calculations (*i.e.*, that the abundances of the ionization states of the element present at any given time are not necessarily the same as those that would be present at the same temperature and density for a system in thermodynamic equilibrium). The ion emissivities were taken from the CHIANTI version 6 database; the elemental abundances were taken from Feldman *et al.* (1992 [25]); the recombination coefficients were taken from Mazzotta *et al.* (1998 [47]) and the ionization coefficients from Dere (2007 [19]).

Table 1 shows the parameters of each of the six runs. In each case, the heating profile took a triangular shape in time, as shown in figure 3-2, with the electrons being preferentially heated. The loop was then allowed to cool, until it reached a minimum electron temperature (the time to do this does not vary much). We then synthesize the emission measure as described in chapter 2, where the lines used for the Pottasch method calculations are given in table 2 (for Hinode-EIS).

The results for the six runs are presented. Figures 3-3 through 3-5

#	t_t	t_R	t_F	E_H	E_{Total}	$t(T_{min})$	b	b_{Pot}
1	10	5	5	0.2	1.0	2530	1.49	2.64
2	30	15	15	0.2	3.0	2500	1.46	2.56
3	60	30	30	0.2	6.0	2550	1.91	1.93
4	120	60	60	0.2	12.0	2920	1.95	2.28
5	300	150	150	0.2	30.0	2910	2.05	1.90
6	600	300	300	0.2	60.0	2940	2.04	2.16

Table 1: The six initial runs done with HYDRAD. In each case, there was one heating event set off in the loop, with a simple triangular heating profile, lasting a total of t_t seconds, with a rise and fall time t_R and t_F seconds each. The heating event had a peak volumetric heating rate of E_H erg s^{-1} cm^{-3}, for a total energy input of E_{Total} erg cm^{-3}. After heating ended, the loop reached its minimum electron temperature T_{min} in $t(T_{min})$ seconds. The emission measure was then found to have a power-law index b from the peak temperature down to about 1 MK, and b_{Pot} calculated using the Pottasch method. See figure 3-2 to see the first heating profile (all the others have the same shape with a longer duration).

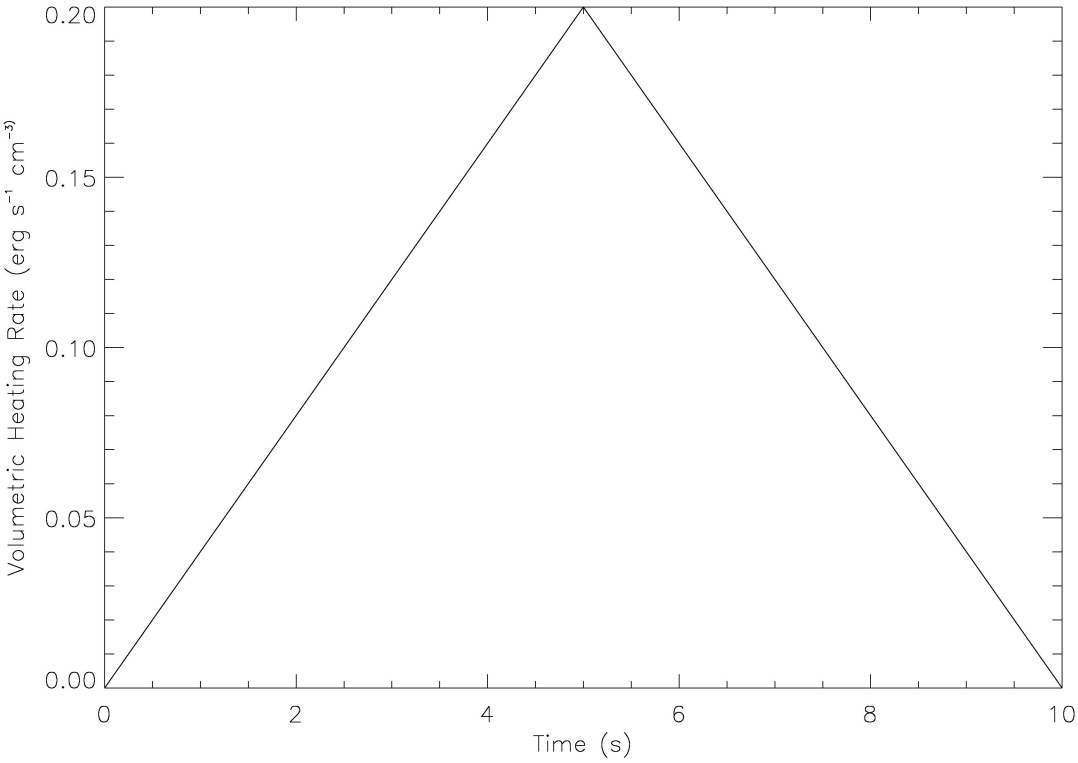

Figure 3-2: The heating profile for the first run. The volumetric heating rate rises up to a peak value E_H in t_R seconds, and then falls back to zero in t_F seconds. The total energy input E_{Total} into the loop is the integral of this curve in time. The other five runs have a similar profile, but longer duration (and thus higher t_R and t_F).

Ion	Wavelength	log T
Mg V	276.579	5.45
Mg VI	268.991	5.65
Mg VI	270.391	5.65
Si VII	275.354	5.80
Mg VII	278.404	5.80
Mg VII	280.745	5.80
Fe IX	188.497	5.85
Fe IX	197.865	5.85
Si IX	258.082	6.05
Fe X	184.357	6.05
Fe XI	180.408	6.15
Fe XI	188.232	6.15
Si X	258.371	6.15
Si X	261.044	6.15
S X	264.231	6.15
Fe XII	192.394	6.20
Fe XII	195.119	6.20
Fe XIII	202.044	6.25
Fe XIII	203.828	6.25
Fe XIV	264.790	6.30
Fe XIV	270.522	6.30
Fe XIV	274.204	6.30
Fe XV	284.163	6.35
S XIII	256.685	6.40
Fe XVI	262.976	6.45
Ca XIV	193.866	6.55
Ca XV	200.972	6.65
Ca XVI	208.604	6.70
Ca XVII	192.853	6.75
Fe XVII	269.494	6.75

Table 2: The 30 emission lines used to compute the predicted Hinode-EIS emission measure, calculated with the Pottasch method. The ion is listed with its laboratory wavelength (in Å) and its formation temperature (in K). The same lines were chosen as in the observational studies of Warren *et al.* (2011 [74]) and Tripathi *et al.* (2011 [67]).

show the mean density and temperature as a function of time and the calculated column emission measure for a sample of the runs. If we fit a line from the peak of each emission measure down to 10^6 K, we find the slopes listed in table 1, where b is the real emission measure slope and b_{Pot} is that found with the Pottasch method.

Figure 3-4 shows a typical loop evolution. After heating begins, the loop has a low density, and as shown in chapter 2, thermal conduction dominates the energy transport as there is little energy loss by radiation. The temperature during heating thus rises rapidly to around 13 MK (slightly more than the 10 MK aimed for). The excess energy will be transported to the lower layers of the atmosphere (specifically the transition region and chromosphere), where the conduction is less effective and it begins to become more optically thick. Further, the chromosphere cannot radiate away all of the excess energy. Thus, the temperature at the top of the chromosphere will increase, causing an increase in pressure, which will drive an upflow (termed chromospheric ablation). Thus, shortly after heating, we see the loop's density increase while the corona cools.

This increase in density then strengthens the radiative losses, eventually overtaking conduction as the dominant cooling mechanism in the

corona. The pressure gradient from the transition region supports the corona, but because the transition region is denser and cooler than the corona, it radiates more strongly, and eventually the pressure gradient weakens enough so that material is allowed to drain from the corona. When this occurs, the loop cools through both radiative loss and a downward-flowing enthalpy flux. This will drive a catastrophic collapse of the loop in terms of both density and temperature, as we see in figure 3-4.

We compare these results to observations of active region loops. Warren *et al.* (2011 [74]) found a power-law index b of 3.26 for their observed active region loop (see figure 1-7). Winebarger *et al.* (2011 [78]) similarly find a value of 3.2 in the same temperature range. Tripathi *et al.* (2011 [67]), studying inter-moss regions, found slopes ranging from 2.05 through 2.70, depending on how they performed background subtraction (see table 2 of their paper). In all cases, these are significantly steeper than the slopes obtained from the simulated emission measures and slightly larger than the predicted Hinode-EIS emission measures, implying that we predict more plasma at lower temperatures than is present in real active region loops.

It is difficult to reconcile our model with the observations. It is

not likely that energy release would occur on much longer time-scales than we have used (*i.e.*, longer than the cooling time-scale or about 10 minutes of energy input). Any single heating event appears to over-estimate the amount of low temperature plasma. As evidenced by the Pottasch method slopes found in this chapter, there are instrumental effects that can alter the slope (see the next chapter for more), but the temperature distribution of the plasma still does not agree with observations. We thus seek an alternative explanation for the heating mechanism occurring in active regions: perhaps the bursts of energy are split into smaller, impulsive bursts.

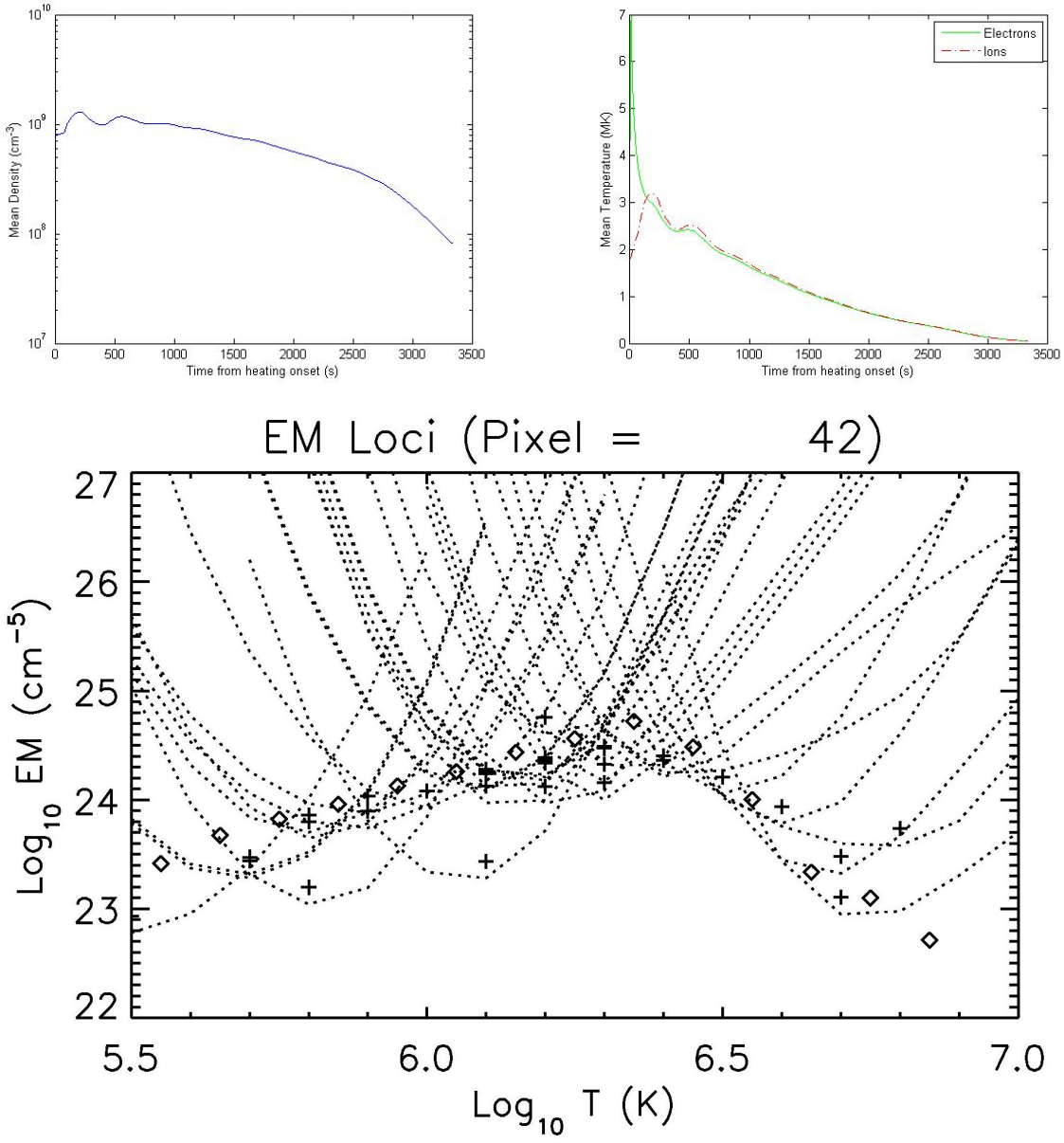

Figure 3-3: Results for the first heating event (10 seconds of heating with a total of 1.0 erg cm^{-3} of energy input). *Top Left:* The mean density in the coronal loop as a function of time. *Top Right:* The mean temperature in the coronal loop as a function of time. *Bottom:* The column emission measure calculated for this heating event, where the diamonds are the real emission measure and the plus signs are for the predicted Hinode-EIS emission measure.

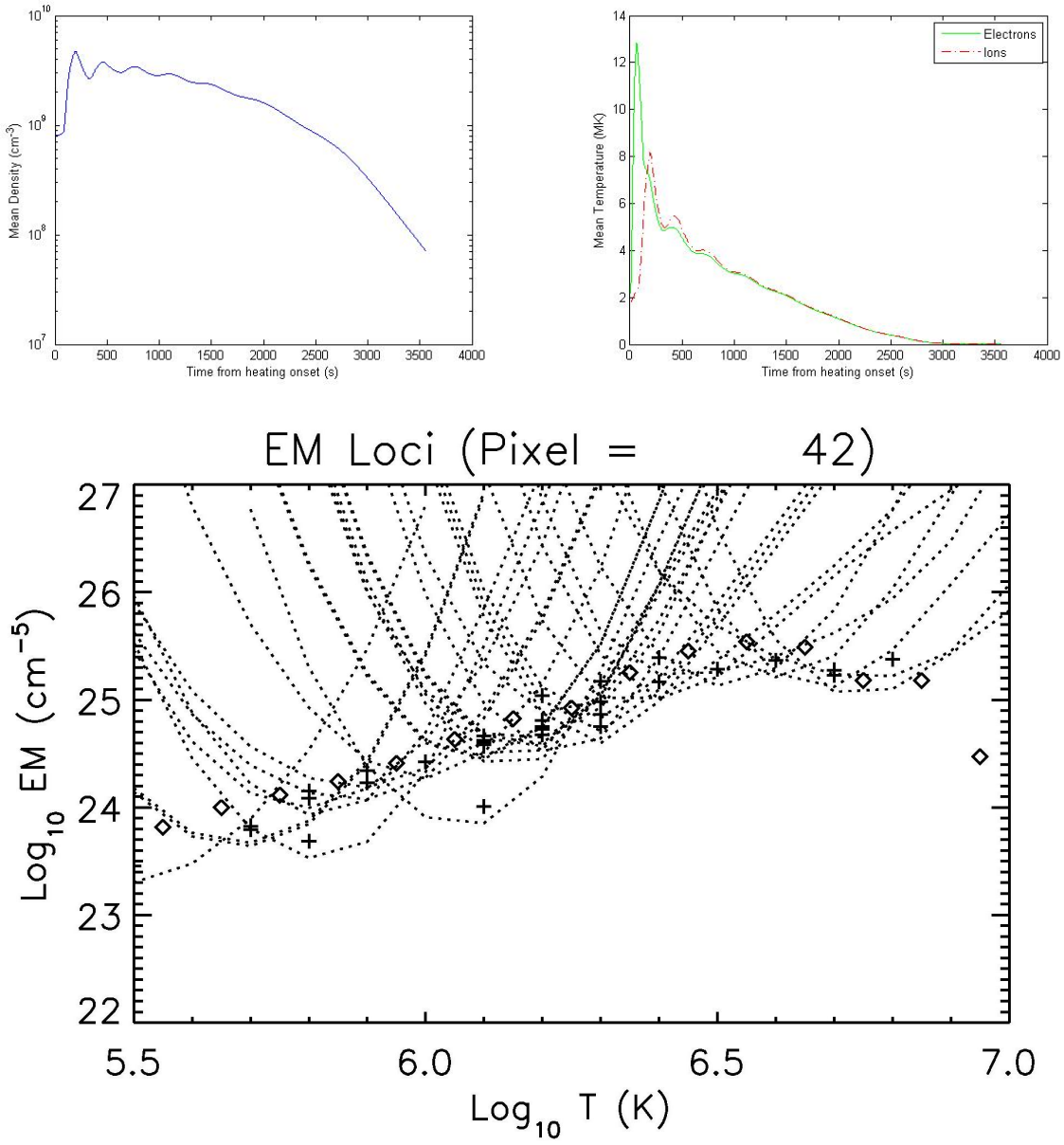

Figure 3-4: Results for the fourth heating event (120 seconds of heating with a total of 12.0 erg cm^{-3} of energy input). *Top Left:* The mean density in the coronal loop as a function of time. *Top Right:* The mean temperature in the coronal loop as a function of time. *Bottom:* The column emission measure calculated for this heating event, where the diamonds are the real emission measure and the plus signs are for the predicted Hinode-EIS emission measure.

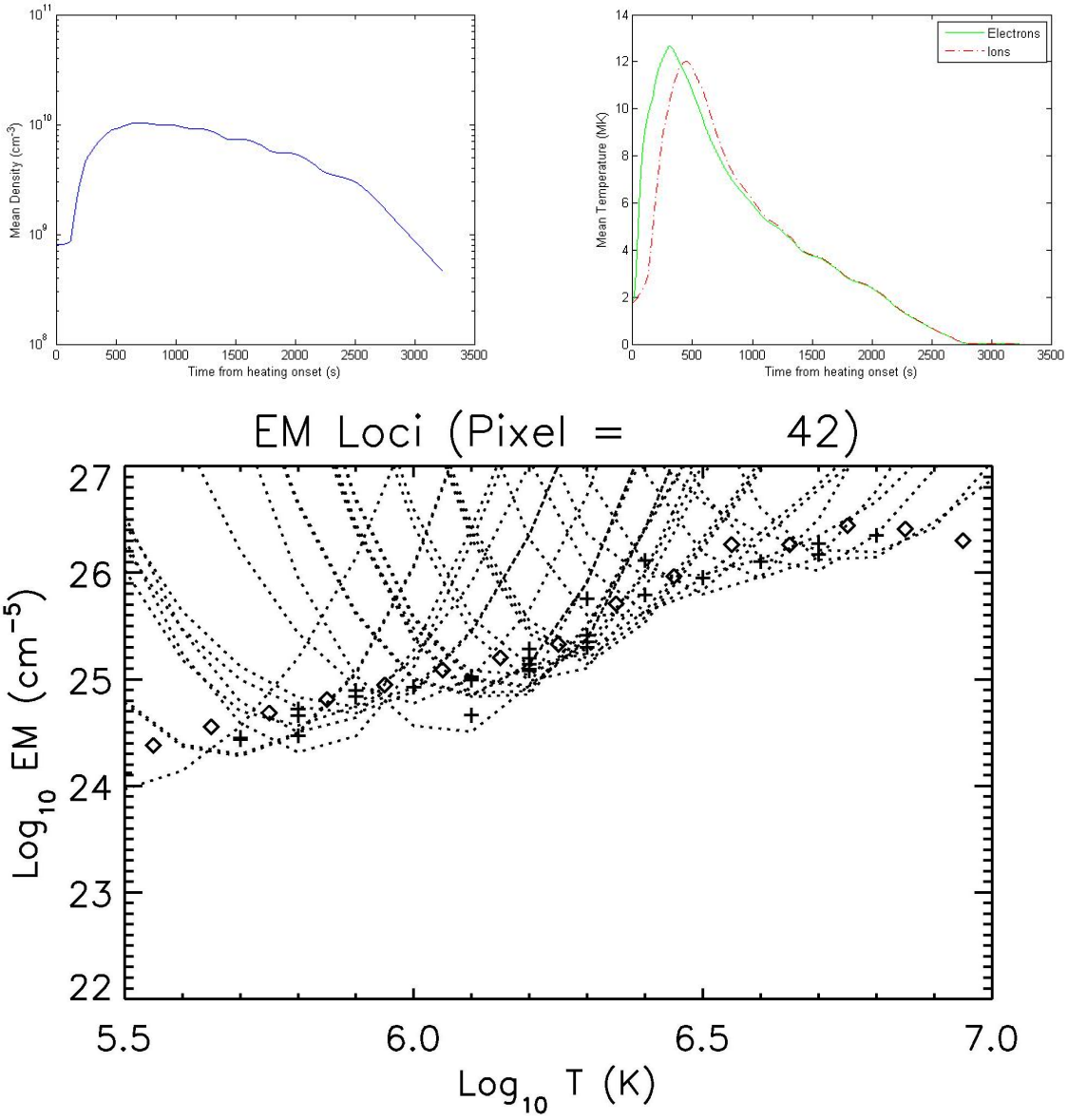

Figure 3-5: Results for the sixth heating event (600 seconds of heating with a total of 60.0 erg cm^{-3} of energy input). *Top Left:* The mean density in the coronal loop as a function of time. *Top Right:* The mean temperature in the coronal loop as a function of time. *Bottom:* The column emission measure calculated for this heating event, where the diamonds are the real emission measure and the plus signs are for the predicted Hinode-EIS emission measure.

4 Heating by repeated nanoflare storms

We have seen that the calculated emission measures for single nanoflare storms have too much emission from low temperature plasma when compared with observations of active region loops, regardless of the duration of the storm. Thus, it seems unlikely that a single heating event is sufficient to explain the observed emission measures. In effect, then, we need more hot strands than "warm" strands along the line-of-sight. We hypothesize that perhaps a series of nanoflare storms, with periods of cooling in between, would increase the high temperature emission relative to the cool emission, which may bring the results closer to observations.

Supposing that the energy release of nanoflares is due to magnetic reconnection from the twisting of magnetic flux bundles, then after a heating event the field lines will be in their lowest energy state. However, (as described in Parker 1988 [51]) the field lines are twisted by random convective motions on the photosphere (where they are rooted), and so the field lines immediately will begin to twist again, effectively recharging the stored energy. Thus, it is only a matter of time before reconnection occurs once again. Lin *et al.* (1984 [42]) found that peri-

odic brightenings in the hard X-rays occur at random intervals around 300 seconds. For our simulations, we used equal intervals ranging from 60 to 300 seconds.

We thus ran 20 new simulations to recreate a succession of nanoflare storms. We divide these simulations into five groups of four, with 5, 10, 15, and 20 nanoflare storm heating events in each group. We call the heating time of an individual event τ_H and the cooling time between each event τ_C. The simulations and their parameters are listed in table 3.

We used a loop of length 100 Mm, with a foot-point height (chromospheric depth) of 10^9 cm, as before. The same initial loop density and temperature profiles were used in all simulations, shown in figure 4-2 (note that these values are slightly different than the profiles used in the previous chapter, although derived in a similar manner). Each individual event had a similar triangular profile (similar to the profile shown in the previous chapter, figure 3-2). The total heating period lasted from the onset of heating at zero seconds time until the last heating event ended (see figure 4-1 for the first simulation consisting of five heating events lasting 60 seconds each with 60 seconds of cooling in between). We treated radiative losses with the piece-wise power-law

function (equation 8, and this is why the initial conditions differ slightly from the previous chapter). We evolved the loop from the onset of the first heating event until the electron temperature reached its minimum value (usually about 3500 s after the last heating event ended). The multi-stranded loop is now constructed from individual strands, some of which have been re-energized multiple times. Again there is one strand for each phase of the evolution of the loop, from the onset of heating to eventual collapse.

The results for the 20 simulations are summarized in table 3. Figures 4-3 through 4-7 show the mean density and temperature profiles as a function of time, as well as the calculated column emission measures, for a sample of the simulations. In these diagrams, the true emission measures are the points represented by diamonds, while the plus signs are for synthetic emission measures that we predicted from Hinode-EIS data at the apex of the loop, calculated using the Pottasch method with 30 different spectral lines (the same as the previous chapter: listed in table 2).

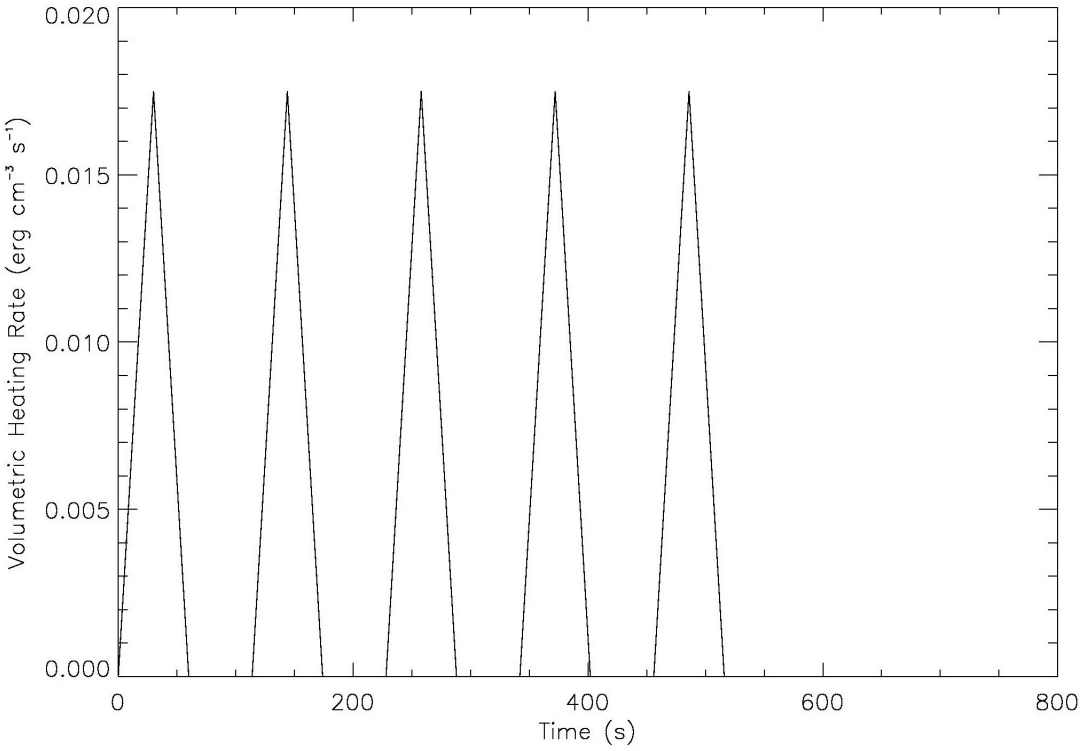

Figure 4-1: The heating input as a function of time for the first simulation, consisting of five heating events lasting 60 seconds each with 60 seconds of cooling in between. The peak volumetric heating rate was 0.0175 erg cm^{-3} s^{-1}. After the last heating event, all heating ceases and the loop is allowed to cool. All of the simulations in this section had a similar profile with the same peak volumetric heating rate, except that the number of heating events varied or the length of heating and cooling varied. As before, we preferentially heated the electrons.

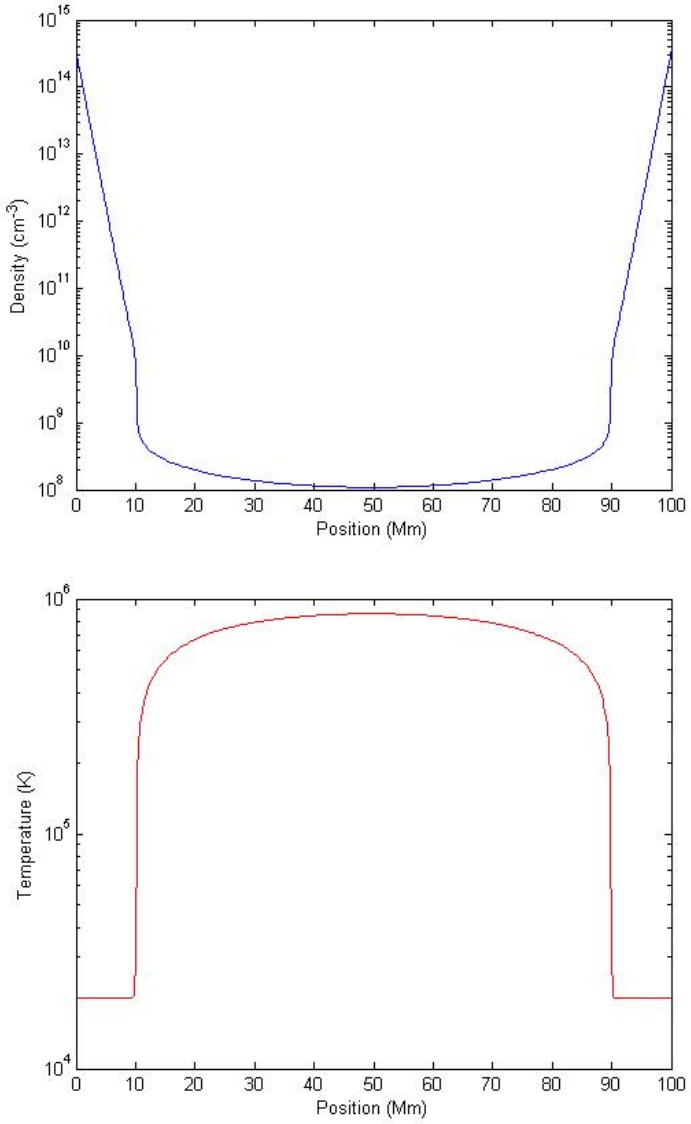

Figure 4-2: The initial density and temperature profiles as a function of position along the coronal loop. Each of the twenty simulations described in this section had the same initial profile. The ions and electrons were initially in thermal equilibrium.

Number	N	τ_H	τ_C	$\frac{\tau_H}{\tau_C}$	T_H	T_C	$\frac{T_H}{T_C}$	b	b_{Pot}
1	5	60	60	1.0	540	4333	.125	1.23	2.54
2	10	60	60	1.0	1140	3939	.289	1.11	1.65
3	15	60	60	1.0	1740	3699	.470	1.53	1.67
4	20	60	60	1.0	2340	3538	.661	1.77	1.95
5	5	60	300	0.2	1500	4198	.357	1.29	2.52
6	10	60	300	0.2	3300	3844	.858	2.16	2.27
7	15	60	300	0.2	5100	3776	1.35	2.57	2.93
8	20	60	300	0.2	6900	3771	1.83	2.84	3.42
9	5	180	180	1.0	1620	3767	.430	1.61	1.68
10	10	180	180	1.0	3420	3453	.990	2.15	2.37
11	15	180	180	1.0	5220	3429	1.52	2.49	2.82
12	20	180	180	1.0	7020	3436	2.04	2.72	3.13
13	5	300	60	5.0	1740	3453	.504	1.66	1.41
14	10	300	60	5.0	3540	3292	1.08	2.09	2.06
15	15	300	60	5.0	5340	3270	1.63	2.30	2.65
16	20	300	60	5.0	7140	3284	2.17	2.44	2.91
17	5	300	300	1.0	2700	3530	.765	1.99	2.19
18	10	300	300	1.0	5700	3448	1.65	2.57	2.95
19	15	300	300	1.0	8700	3446	2.52	2.88	3.39
20	20	300	300	1.0	11700	3457	3.38	3.07	3.70

Table 3: The results of the 20 simulations done for multiple nanoflare storm heating events. The second column N is the number of heating events. The third and fourth columns τ_H and τ_C are the individual heating time scale and cooling time scale between events (in seconds). The fifth column is their ratio. The sixth column is the heating time T_H from the onset of the first event until the end of the last event (in seconds). The seventh column is the cooling time T_C from the end of the last heating event until the minimum electron temperature is reached (in seconds). The eighth column is their ratio. The ninth and tenth column are the calculated slopes b for the real emission measure and the predicted observable emission measure (using the Pottasch method), respectively.

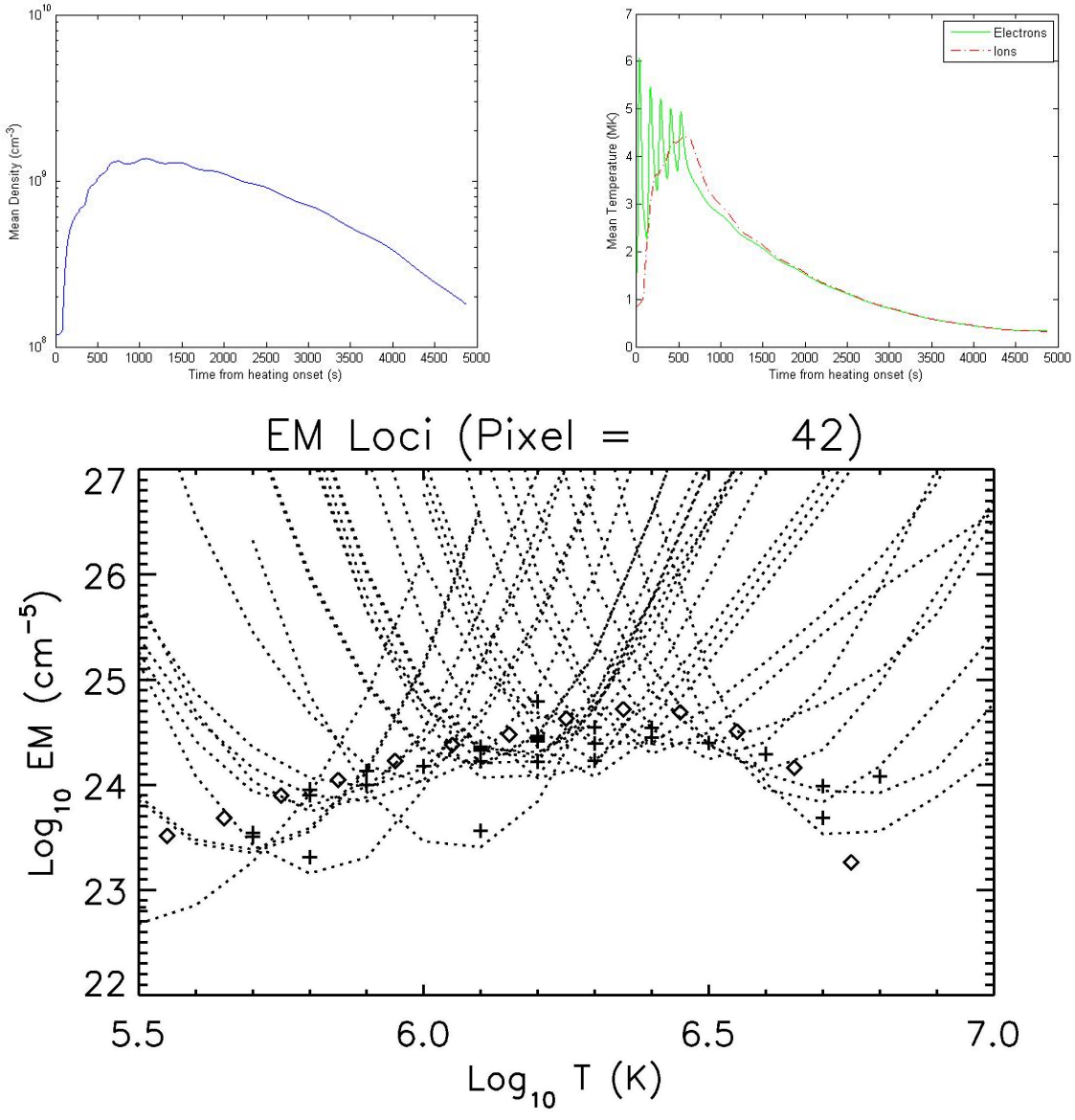

Figure 4-3: The results for the first simulation (five heating events lasting 60 seconds, with 60 seconds of cooling in between). *Top Left:* The mean density in the coronal loop as a function of time. *Top Right:* The mean temperature in the coronal loop as a function of time. *Bottom:* The column emission measure as a function of temperature. The diamonds represent the real emission measure; the plus signs mark the predicted observable emission measure as might be seen at the loop apex with Hinode-EIS.

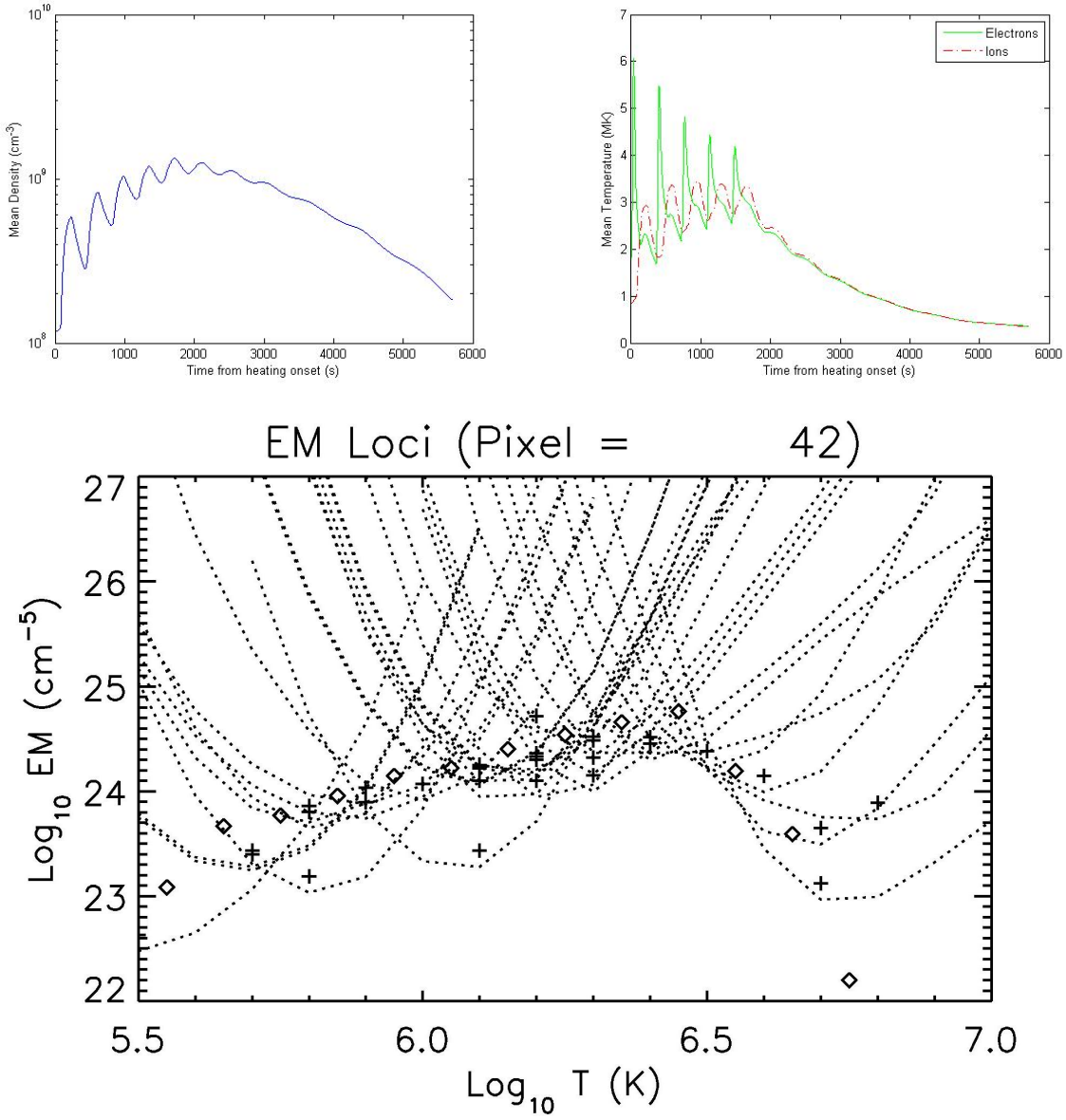

Figure 4-4: The results for the fifth simulation (five heating events lasting 60 seconds, with 300 seconds of cooling in between). *Top Left:* The mean density in the coronal loop as a function of time. *Top Right:* The mean temperature in the coronal loop as a function of time. *Bottom:* The column emission measure as a function of temperature. The diamonds represent the real emission measure; the plus signs mark the predicted observable emission measure as might be seen at the loop apex with Hinode-EIS.

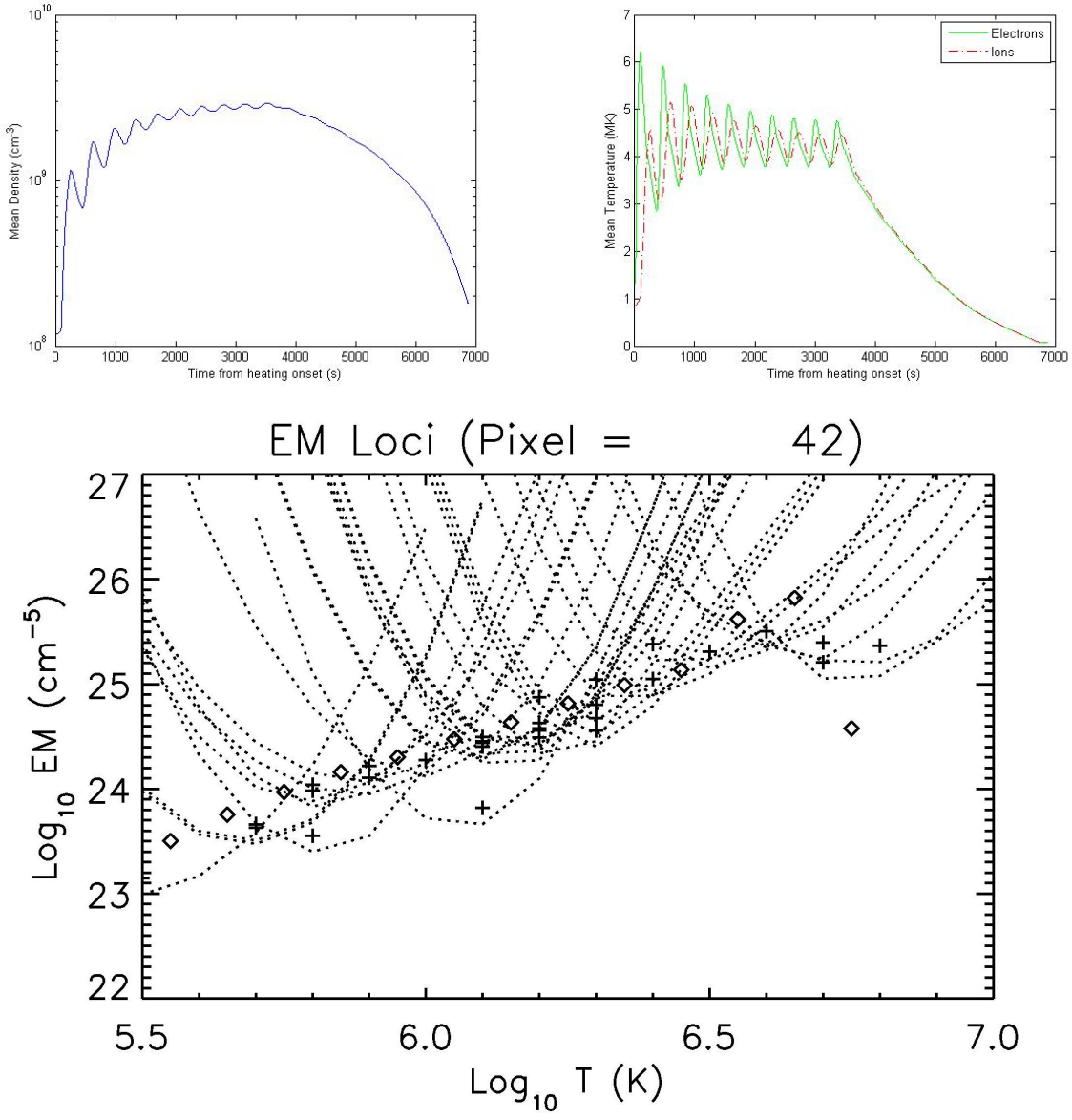

Figure 4-5: The results for the tenth simulation (ten heating events lasting 180 seconds, with 180 seconds of cooling in between). *Top Left:* The mean density in the coronal loop as a function of time. *Top Right:* The mean temperature in the coronal loop as a function of time. *Bottom:* The column emission measure as a function of temperature. The diamonds represent the real emission measure; the plus signs mark the predicted observable emission measure as might be seen at the loop apex with Hinode-EIS.

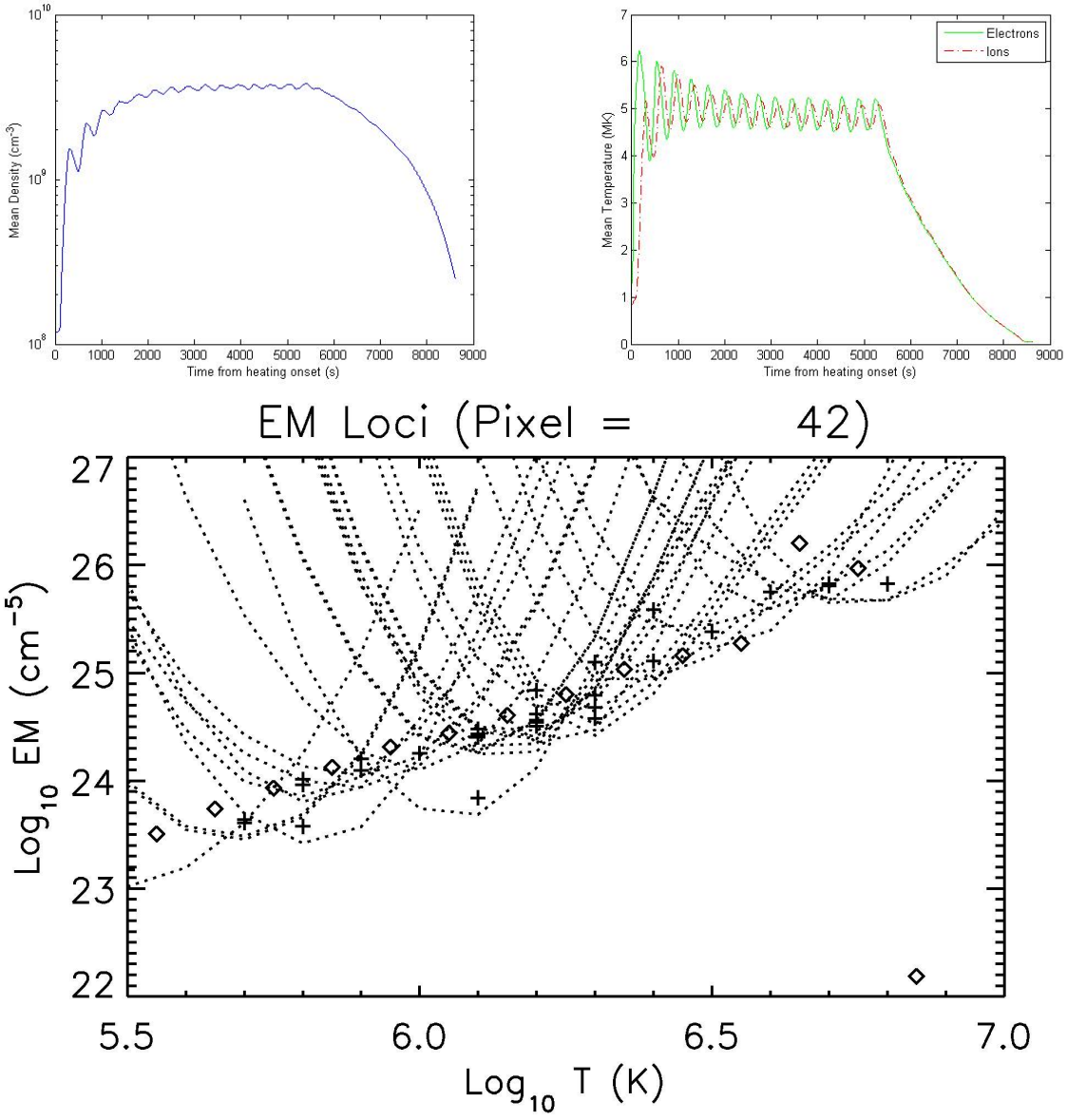

Figure 4-6: The results for the fifteenth simulation (fifteen heating events lasting 300 seconds, with 60 seconds of cooling in between). *Top Left:* The mean density in the coronal loop as a function of time. *Top Right:* The mean temperature in the coronal loop as a function of time. *Bottom:* The column emission measure as a function of temperature. The diamonds represent the real emission measure; the plus signs mark the predicted observable emission measure as might be seen at the loop apex with Hinode-EIS.

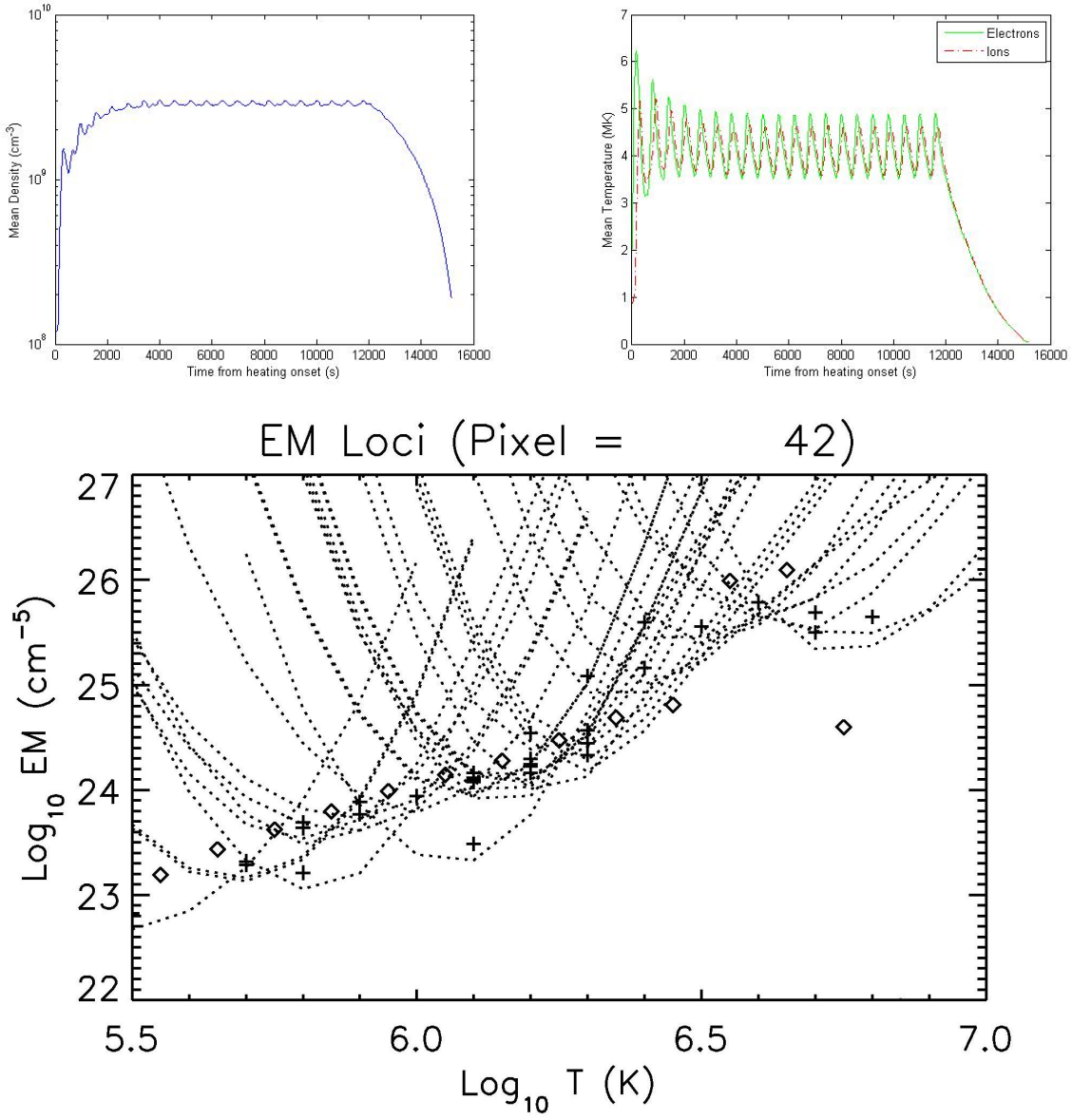

Figure 4-7: The results for the twentieth simulation (twenty heating events lasting 300 seconds, with 300 seconds of cooling in between). *Top Left:* The mean density in the coronal loop as a function of time. *Top Right:* The mean temperature in the coronal loop as a function of time. *Bottom:* The column emission measure as a function of temperature. The diamonds represent the real emission measure; the plus signs mark the predicted observable emission measure as might be seen at the loop apex with Hinode-EIS.

From these results, it would appear that the ratio of the total heating time T_H (from the onset of the first event to the end of the last event) to the total cooling time T_C (from the end of the last event until the minimum electron temperature is reached) dominates the calculated slopes. Specifically, the larger this ratio is, the larger the slopes will be (whether for the real or predicted observable emission measure). Since the cooling time is nearly the same in every case (being primarily a function of loop length which is the same in every case), in effect, the longer the heating mechanism is active, the larger the slope becomes. Physically this means that the amount of plasma at high temperatures increases relative to that at lower temperatures (steepening the slope). The pauses in between heating events are important though: recall the high-frequency heating simulation of Warren *et al.* (2011 [74]) where they did not allow the plasma time to cool in between events, and thereby obtained an essentially isothermal loop. With the recent work of Viall & Klimchuk (2012 [73]), it might be possible to diagnose the periodicity and length of the individual heating and cooling events. Using SDO-AIA, they have created time-lag maps that show how long it takes a loop to cool by plotting the strength of different spectral lines at different formation temperatures as functions of time. If there

is periodicity in the data (for example, if the high temperature channels emit periodically every 5 minutes), then we might be able to constrain τ_H and τ_C.

Figure 4-8 demonstrates the trend (we do not attempt a curve-fit, as it is not clear whether that trend is linear, quadratic, or something else). Further, note that in 18 of the 20 cases, the predicted observable emission measure slope is greater than the real emission measure slope (see below for an explanation). Most importantly, we see that many of the simulations obtain a power-law index b within the observed range, unlike the simulations in the previous chapter.

Note that in all of the emission measure figures, there are two low-hanging data Pottasch method data points (specifically Si IX at 258.082 Å formed at $10^{6.05}$ K and Mg VII at 280.745 Å formed at $10^{5.8}$ K). These two points appear to be out of line with the rest of the curve, and we suggest that the contribution functions were calculated incorrectly. The contribution function, shown in equation 12, might be defined as:

$$G(T) = C^e_{g,j} \frac{n(X^{+m})}{n(X)} \tag{40}$$

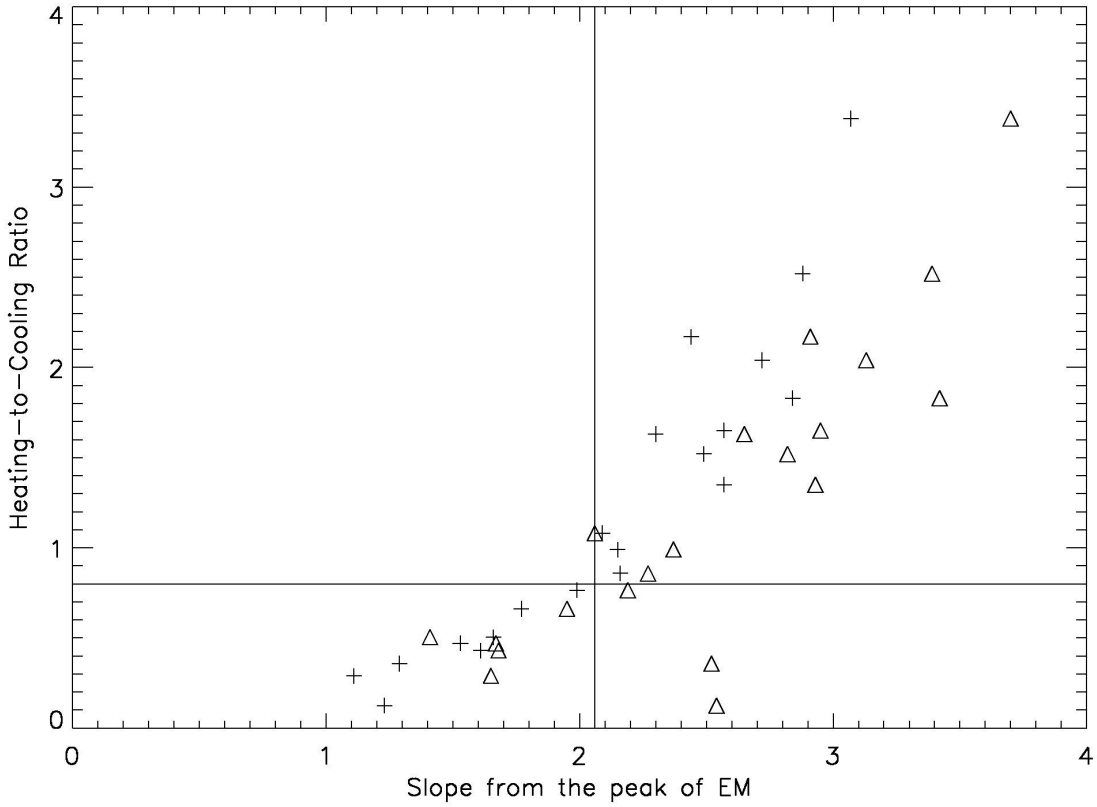

Figure 4-8: The ratio of the total heating time T_H to total cooling time T_C versus the calculated emission measure slopes b (from the peak of the emission down to 10^6 K). The plus signs are for the real emission measure calculations, while the triangles are the predicted observable emission measure calculations. In both cases, there is a clear positive correlation. The upper right quadrant, marked by the lines, roughly indicates where the observations lie.

where $C^e_{g,j}$ is the collisional excitation rate coefficient from the ground state to state j of an ion, $n(X^{+m})$ is the number density of ions of charge $+m$ of element X, and $n(X)$ is the number density of element X (including all ions of the element). Unfortunately in practice, we do not know the electron density and must venture an estimate to calculate the contribution function. Following previous authors (*e.g.*, Tripathi *et al.* 2011 [67]), for the 20 simulations in this section, we initially tried a density of 10^{10} cm^{-3}. Although we still do not know the true density, it seems more likely that 10^9 cm^{-3} is a much better estimate, as we now demonstrate.

We have recalculated the Pottasch method emission measure for all 20 simulations presented in this chapter, using a density of 10^9 cm^{-3}. The results are summarized in table 4 and figure 4-9. Also, figure 4-10 shows the newly calculated emission measure for the first simulation (compare to figure 4-3). The recalculated Pottasch slopes are closer to the true slopes, although they are still larger in general, suggesting that there may be an inherent observational bias for Hinode-EIS. We caution that the density 10^9 cm^{-3} is still an estimate and that a more accurate value might bring the Pottasch slopes even closer to the true values.

The calculations from this chapter have shown that repeating nanoflares are a viable explanation for the source of heating of coronal loops. As noted in the previous chapter, the observed slopes range from slightly over $b = 2$ to around $b = 3.26$. From the previous chapter we can conclude that any individual (temporally isolated) heating event would not explain the observed emission measures in active regions, but that if the heating events are repeated such that the loop temperature does not fall significantly in between, the emission measures are in line with the observations. Thus, impulsive heating could power active regions in the corona.

Number	N	τ_H	τ_C	$\frac{\tau_H}{\tau_C}$	T_H	T_C	$\frac{T_H}{T_C}$	b	b_{Pot}
1	5	60	60	1.0	540	4333	.125	1.23	0.88
2	10	60	60	1.0	1140	3939	.289	1.11	1.49
3	15	60	60	1.0	1740	3699	.470	1.53	1.77
4	20	60	60	1.0	2340	3538	.661	1.77	1.97
5	5	60	300	0.2	1500	4198	.357	1.29	1.15
6	10	60	300	0.2	3300	3844	.858	2.16	2.10
7	15	60	300	0.2	5100	3776	1.35	2.57	2.76
8	20	60	300	0.2	6900	3771	1.83	2.84	3.26
9	5	180	180	1.0	1620	3767	.430	1.61	1.81
10	10	180	180	1.0	3420	3453	.990	2.15	2.24
11	15	180	180	1.0	5220	3429	1.52	2.49	2.69
12	20	180	180	1.0	7020	3436	2.04	2.72	3.00
13	5	300	60	5.0	1740	3453	.504	1.66	1.38
14	10	300	60	5.0	3540	3292	1.08	2.09	2.03
15	15	300	60	5.0	5340	3270	1.63	2.30	2.40
16	20	300	60	5.0	7140	3284	2.17	2.44	2.65
17	5	300	300	1.0	2700	3530	.765	1.99	2.20
18	10	300	300	1.0	5700	3448	1.65	2.57	2.82
19	15	300	300	1.0	8700	3446	2.52	2.88	3.26
20	20	300	300	1.0	11700	3457	3.38	3.07	3.57

Table 4: The same as the previous table (table 3), except that the Pottasch slope b_{Pot} has been recalculated using a density of $n = 10^9$ cm^{-3}. The slopes are now closer in line with the true slopes b, but they are still in general higher.

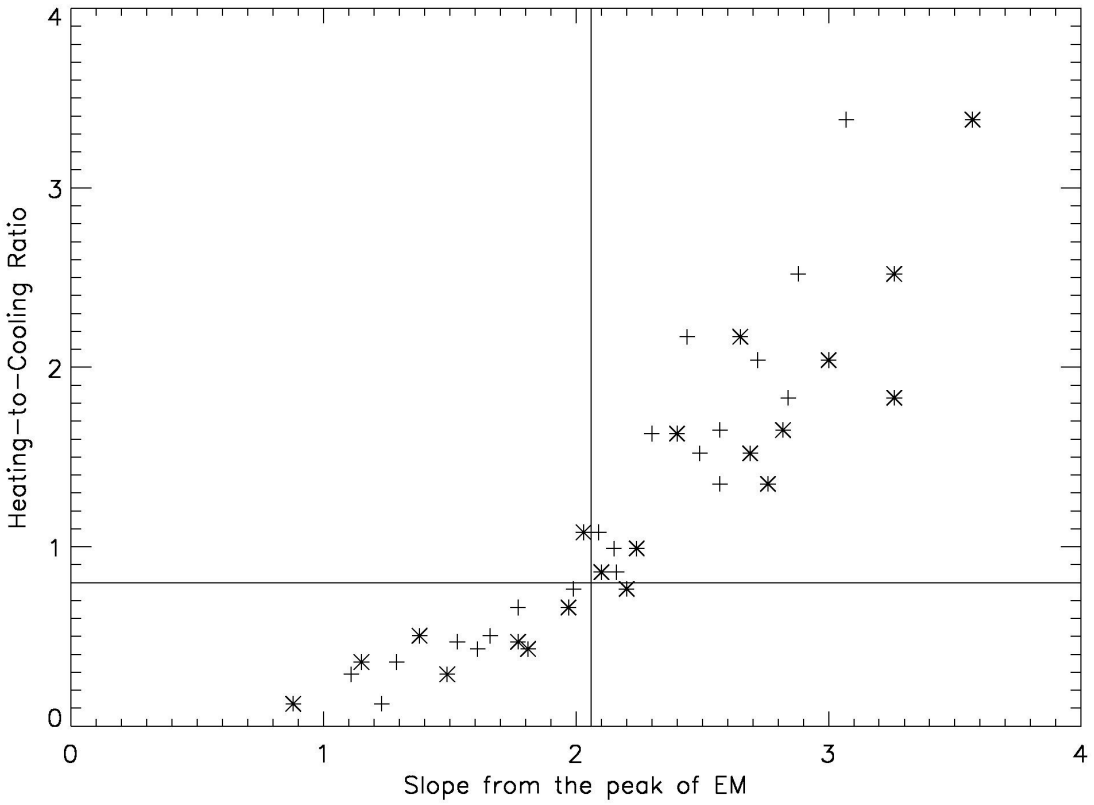

Figure 4-9: The same as figure 4-8, except that the Pottasch slopes have been calculated using a density of $n = 10^9$ cm^{-3}. The true slopes are the plus signs, while the Pottasch slopes are the asterisks. By recalculating, we have brought the two slopes closer in line with each other, although the Pottasch values are still higher in general, suggesting that there may be an inherent observational bias.

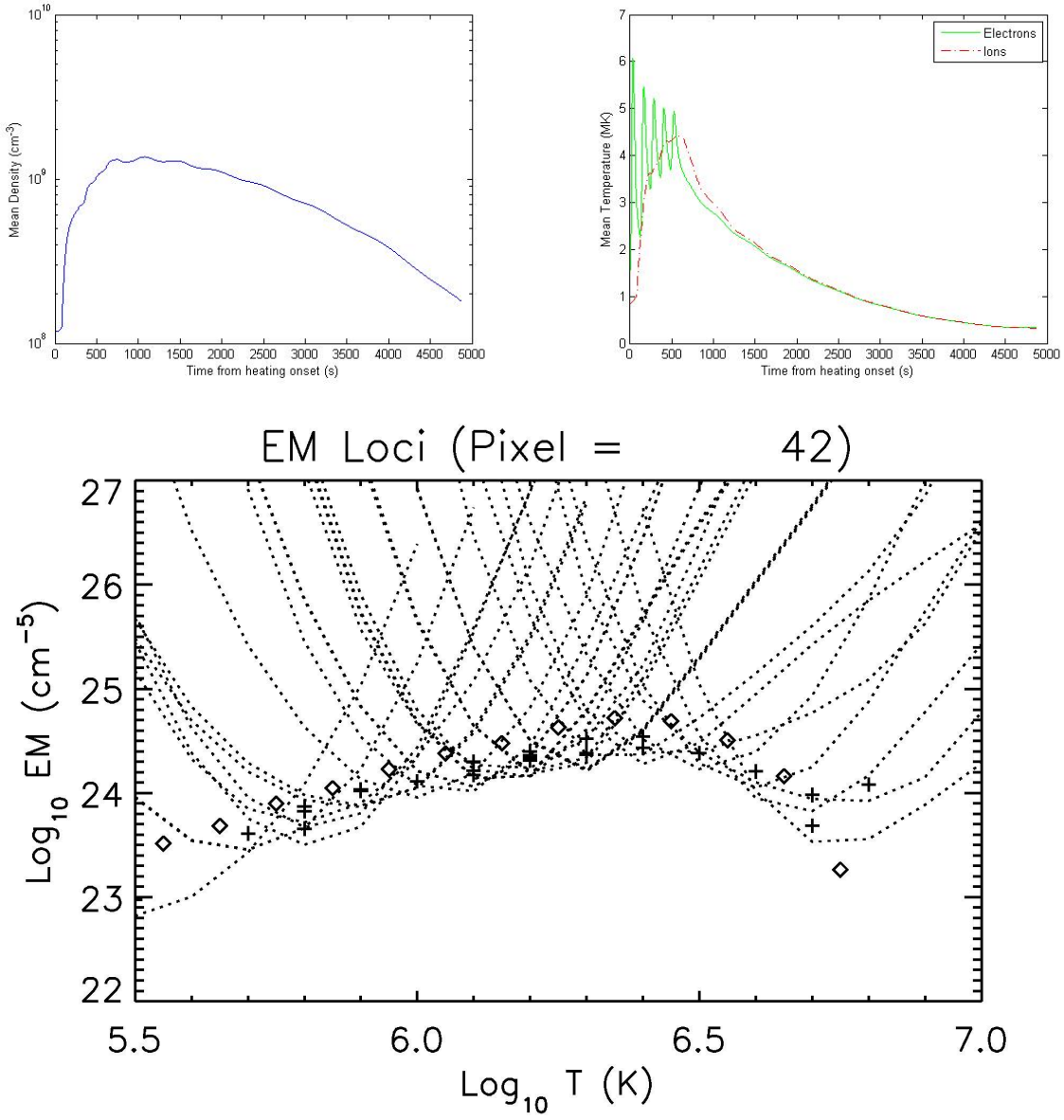

Figure 4-10: The same as figure 4-3 except that the Pottasch slopes (plus signs) have been recalculated using a density of $n = 10^9$ cm^{-3}. Compare this to figure 4-3 and note that the low-hanging emission lines have been brought in line with the rest of the emission measure curve.

5 Doppler Shift Measurements

In section 1.3, an apparently contradictory feature of coronal loops was briefly discussed. Since the work of Rosner *et al.* (1978 [58]), it has been known X-ray loops in active regions can emit radiation steadily for long periods of time (hours or more), which suggests they are being steadily heated. On the other hand, Tripathi *et al.* (2009 [66]), for example, have observed strong down-flows in a well-resolved active region loop, the flows being stronger near the foot-points. In other words, the loop was draining material, thus cooling through an enthalpy flux (in addition to its radiative losses; Bradshaw & Cargill 2010 [13]). However, if the loops are cooling, then they must have been heated at some earlier point in time and we expect an up-flow from the chromosphere into the corona (see figure 3 of Tripathi *et al.* 2009 [66] for an example). The dynamical activity in loops does not appear to be consistent with steady heating.

In the previous chapter, we found that repeated, impulsive heating events can explain the observed emission measure properties of active region loops. We now wish to test the heating mechanism against the observed flows in the loops to see if repeating nanoflare storms

can explain both the emission measure and the dynamical behavior of observed loops. In the previous chapter, in order to calculate the synthesized observable emission measures, we had to build up a spectrum from the 30 spectral lines we chose to include in our study (listed in table 2). We use the standard (non-relativistic) Doppler shift formula to calculate the flow speeds ($\frac{v}{c} = \frac{\Delta\lambda}{\lambda}$) for all the lines in each simulation.

An example set of results for the first simulation of the previous chapter (5 events of 60 seconds heating and 60 seconds cooling) are shown in table 5, figure 5-1, and figure 5-2. Table 5 shows the ion names, rest wavelengths (in Å), formation temperatures (in K), Doppler shift velocities (in km/s), and peak intensities (in DN pixel^{-1} s^{-1} Å^{-1}) as might be seen by Hinode-EIS in a detector pixel that contains chromosphere, transition region, and coronal material along the line-of-sight. Note that intensities are generally reported as total intensities, rather than peak intensities, although it should not affect the conclusions of the present work. By convention, a negative velocity indicates a blue-shift (up-flow), while a positive velocity indicates a red-shift (down-flow). Figure 5-1 shows the synthesized spectrum. Finally, figure 5-2 plots the formation temperature of the lines against their Doppler shift velocities, showing that the lower temperature lines

tend to red-shifted, and the hotter lines tend to be more and more strongly blue-shifted.

The results for the other simulations are similar, but there are a few important details to note. Compare figure 5-3, the temperature versus velocity plot for the twelfth simulation (20 events of 180 seconds heating and 180 seconds cooling), to figure 5-2. The slope of the line is much less steep, and there are 5 points that appear not to follow the trend. The five outliers are: Si VII (275.354 Å), Fe XI (188.232 Å), Fe XIII (203.828 Å), Ca XVII (192.853 Å), and Fe XVII (269.494 Å). These outliers can be explained by noting that they have broader contribution functions $G(T)$ than the others, and the lower temperature and higher density component dominates the line-of-sight contributions. For example, note that in table 5, the intensities of the Fe XI lines at $10^{6.15}$ K are stronger than the other lines at the same formation temperature, due to the broad contribution function of Fe XI. In all 20 simulations, the five ions listed above are consistently and significantly out of line with the overall trend.

The slope of the line in these velocity versus temperature plots depends primarily on the total cooling time T_C (the time from the end of the last heating event to the time of the minimum electron

Number	Ion	Wavelength	log T	Velocity	Peak Intensity
1	MgV	276.579	5.45	8.44	1.68e+000
2	MgVI	268.991	5.65	5.92	2.47e+000
3	MgVI	270.391	5.65	8.43	5.03e+000
4	SiVII	275.354	5.80	13.59	8.12e+000
5	MgVII	278.404	5.80	4.30	3.41e+000
6	MgVII	280.745	5.80	1.73	1.32e+000
7	FeIX	188.497	5.85	5.10	1.49e+001
8	FeIX	197.865	5.85	-0.76	1.41e+001
9	SiIX	258.082	6.05	-1.06	7.52e-001
10	FeX	184.537	6.05	1.61	9.67e+000
11	FeXI	180.408	6.15	-1.83	6.42e+000
12	FeXI	188.232	6.15	16.57	3.34e+001
13	SiX	258.371	6.15	-5.81	3.19e+000
14	SiX	261.044	6.15	-6.20	1.23e+000
15	SX	264.231	6.15	-5.78	1.21e+000
16	FeXII	192.394	6.20	-6.85	2.49e+001
17	FeXII	195.119	6.20	-4.01	9.43e+001
18	FeXIII	202.044	6.25	-11.73	4.75e+000
19	FeXIII	203.828	6.25	-24.13	5.34e+000
20	FeXIV	264.790	6.30	-17.66	2.58e+000
21	FeXIV	270.522	6.30	-18.40	1.49e+000
22	FeXIV	274.204	6.30	-18.58	2.34e+000
23	FeXV	284.163	6.35	-28.04	3.18e+000
24	SXIII	256.685	6.40	-36.21	9.56e-002
25	FeXVI	262.976	6.45	-35.69	9.14e-002
26	CaXIV	193.866	6.55	-45.14	2.92e-002
27	CaXV	200.972	6.65	-51.76	1.18e-003
28	CaXVI	208.604	6.70	-62.08	1.04e-005
29	CaXVII	192.853	6.75	-55.03	1.70e-006
30	FeXVII	269.494	6.75	-31.37	1.89e-004

Table 5: The properties of the 30 spectral lines for the first simulation (5 events of 60 seconds heating and 60 seconds cooling). The values are calculated for the second pixel of the virtual detector, corresponding to the upper chromosphere (foot-point). Wavelength in Å, formation temperature in K, velocity in km/s, and intensity in DN pixel^{-1} s^{-1} Å^{-1}.

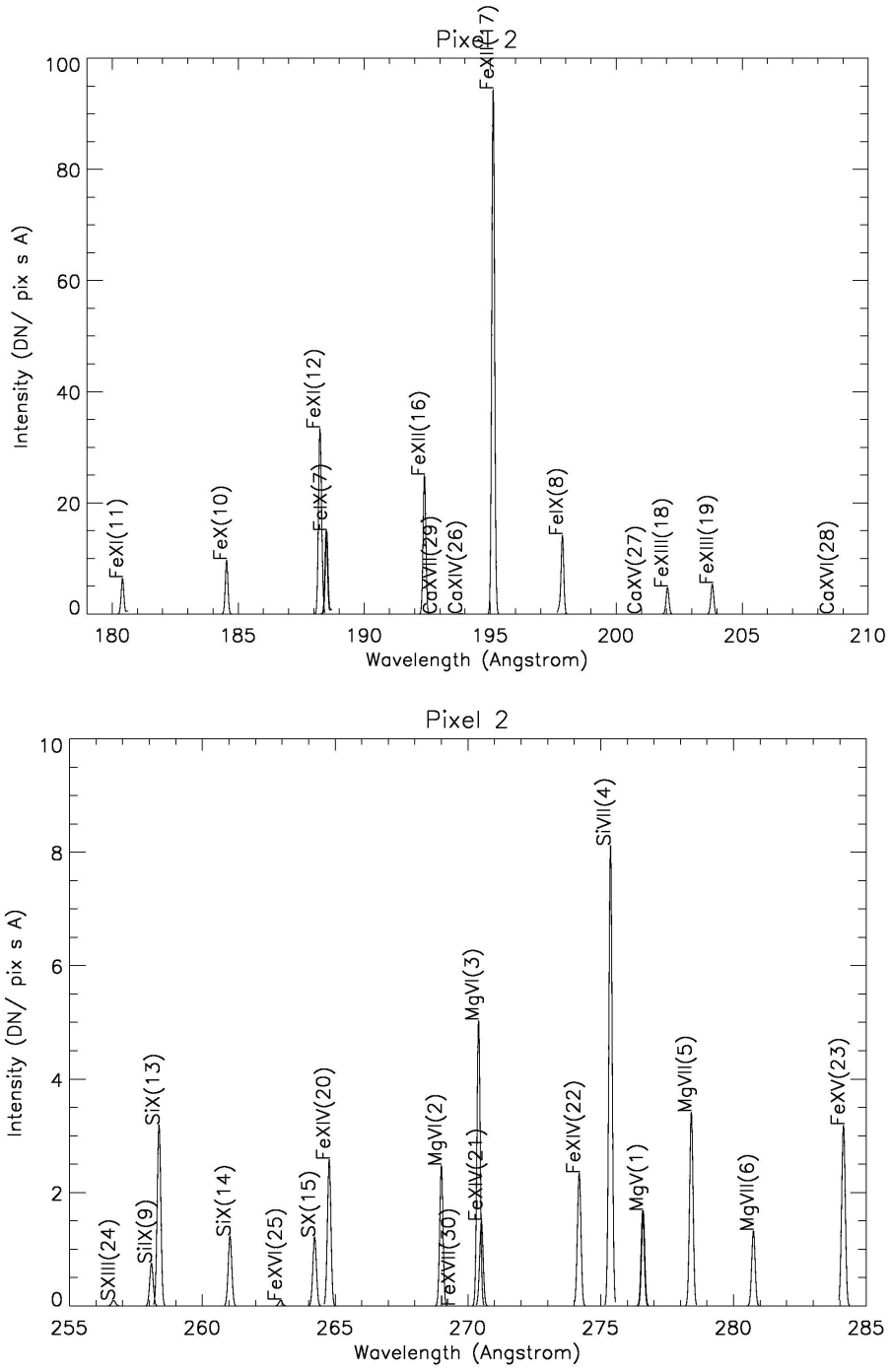

Figure 5-1: The synthesized spectrum for the first simulation, as might be seen by Hinode-EIS. The lines are labeled by their ion name and their number in table 5.

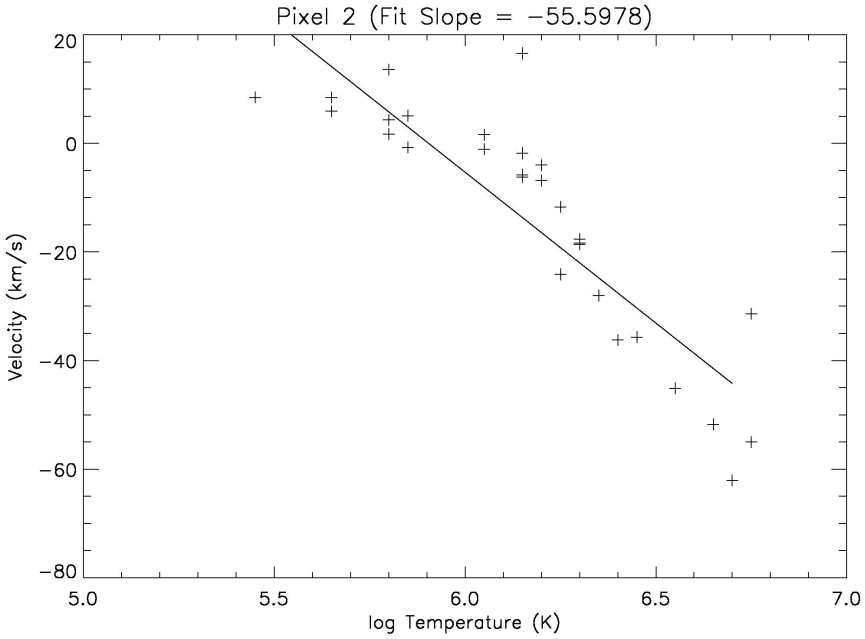

Figure 5-2: The formation temperature versus Doppler shift velocity for the 30 spectral lines, for the first simulation (5 events of 60 seconds heating and 60 seconds cooling). The values are calculated for the second pixel of the virtual detector, which contains emission from the chromosphere, transition region, and corona along the line-of-sight. By convention, a positive velocity indicates a red-shift and a negative velocity a blue-shift. The linear fit was performed while ignoring the 5 outliers identified in the text.

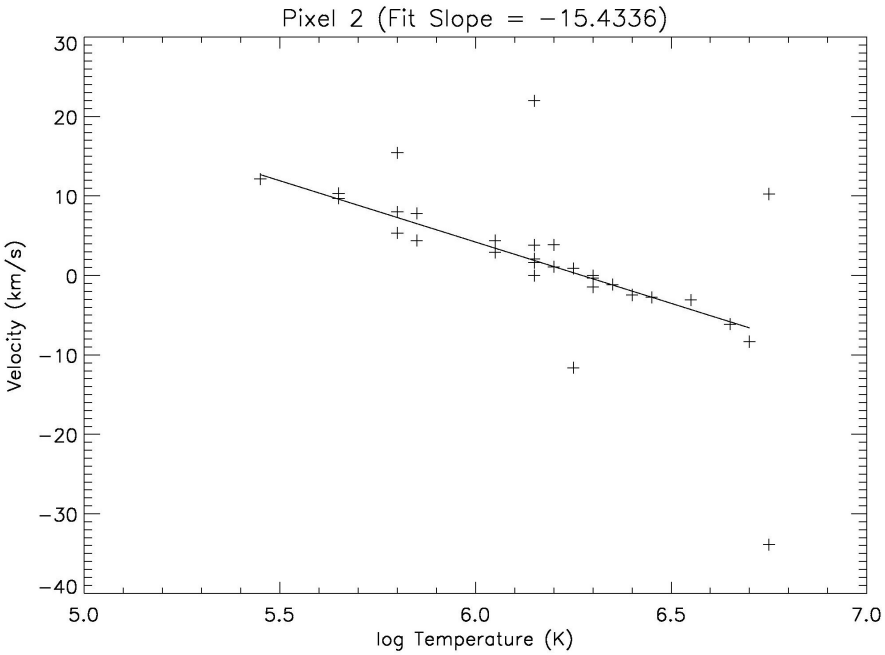

Figure 5-3: The formation temperature versus Doppler shift velocity for the 30 spectral lines, for the twelfth simulation (20 events of 180 seconds heating and 180 seconds cooling). The values are calculated for the second pixel of the virtual detector, which contains emission from the chromosphere, transition region, and corona along the line-of-sight. By convention, a positive velocity indicates a red-shift and a negative velocity a blue-shift. The linear fit was performed while ignoring the 5 outliers identified in the text.

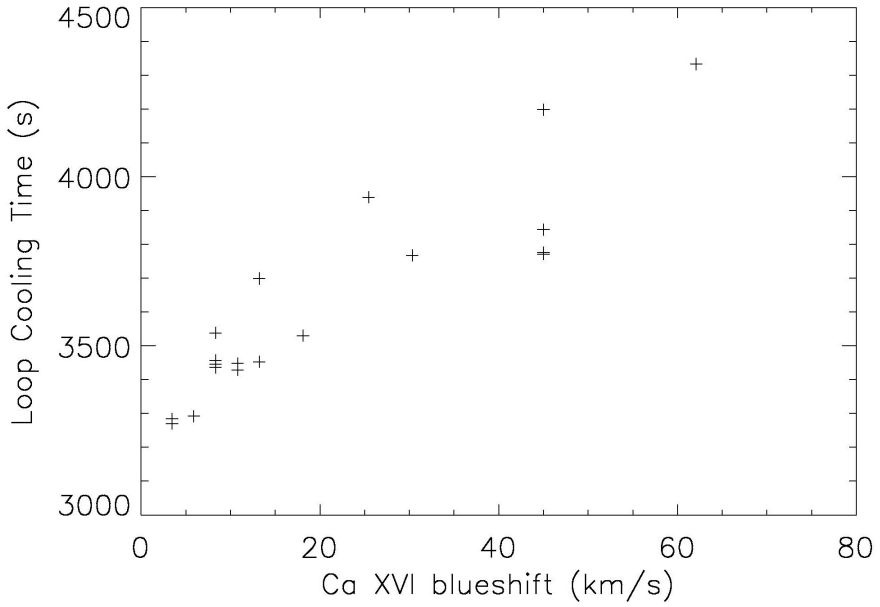

Figure 5-4: The blue-shift of the Ca XVI line at 208.604 Å, formed at $10^{6.70}$ K, versus the total cooling time T_C of the loop.

temperature). Figure 5-4 shows a clear trend between the cooling time and the magnitude of the blue-shift velocity of the Ca XVI line at 208.604 Å(formed at $10^{6.70}$ K). That is, the faster a loop cools, the weaker the up-flows will be. Contrast this with figure 5-5 which shows no correlation between the blue-shift and the heating-to-cooling ratio (that is, total heating time over the total cooling time). Similarly, the red-shifts of the cooler lines depend on the total cooling time as well, as in figure 5-6, plotting against the red-shift of the Mg V line at 276.579 Å. In other words, the faster a loop cools, the stronger the down-flows will be.

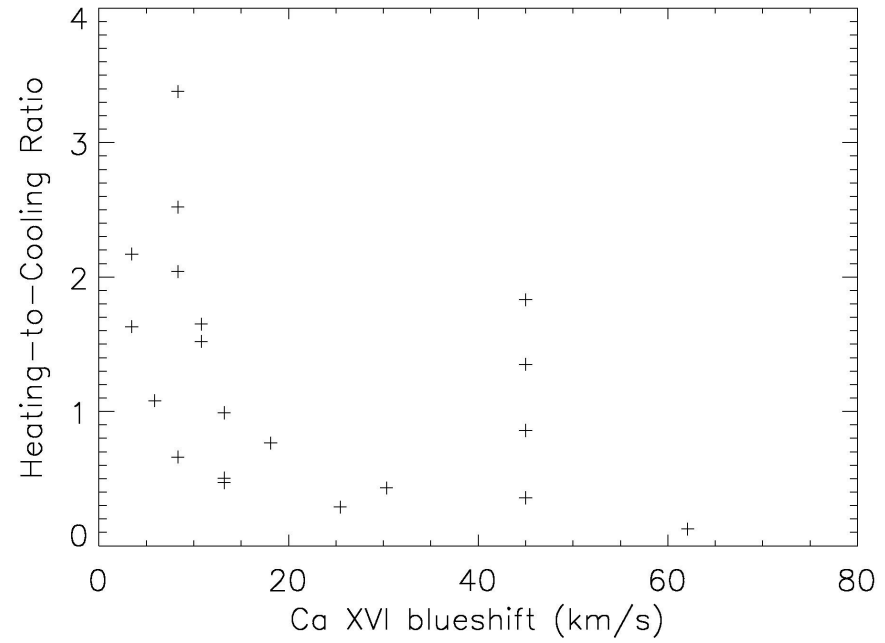

Figure 5-5: The blue-shift of the Ca XVI line at 208.604 Å, formed at $10^{6.70}$ K, versus the ratio of the total heating time to total cooling time of the loop. Note that there is no correlation.

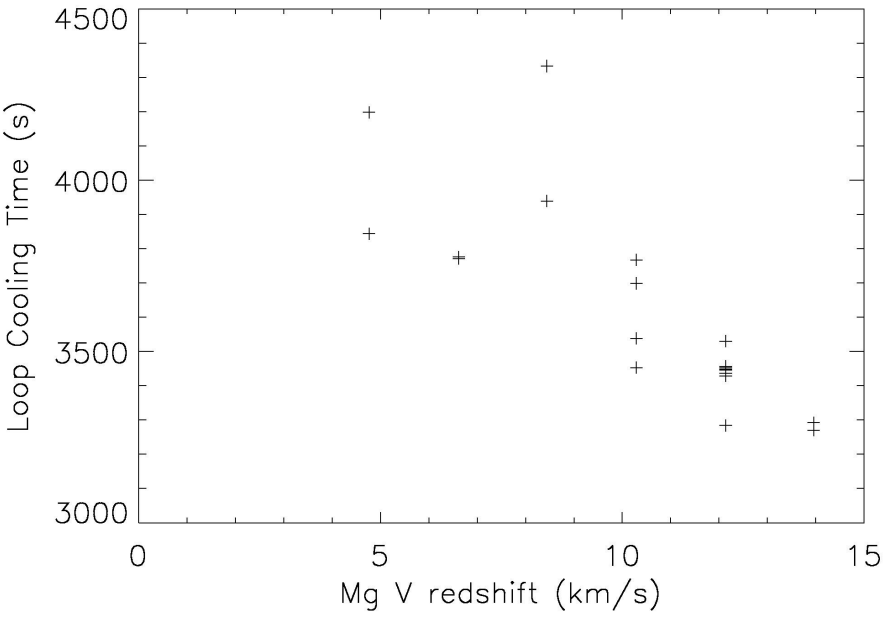

Figure 5-6: The red-shift of the Mg V line at 276.579 Å, formed at $10^{5.45}$ K, versus the total cooling time T_C of the loop.

Why do these depend on the total cooling time of the (electron) temperature? After the heating events cease, the cooling occurs primarily through an enthalpy flux (down-flow) out of the corona and losses through radiation. Bradshaw & Cargill (2005 [11]; 2010 [13]) showed that for a loop cooling through a combination of enthalpy flux and radiation, a scaling law $T \propto n^{\delta}$ exists for which

$$\delta = (\gamma - 1) + \frac{\tau_\nu}{\tau_R} = (\gamma - 1) + \frac{(\gamma - 1) n \chi T^{\alpha - 1}}{2 k_B \frac{\partial v}{\partial s}} \tag{41}$$

where γ is the adiabatic index, τ_ν the draining time-scale ($= 1/\frac{\partial v}{\partial s} \sim L/v_C$ for some characteristic draining speed v_C), and τ_R is the radiation time-scale. The loops which cool the fastest are those which reach a higher density before the heating ends, and so the radiative losses ($\propto n^2$) are significantly stronger, particularly in the transition region where the density increases orders of magnitude over the corona. The greater radiative losses (faster cooling) require more energy to be supplied from the corona, which can only be satisfied by an increase in the enthalpy flux. Therefore, the red-shifted lines, due to a bulk flow out of the corona, must therefore be correlated with the cooling time (*i.e.*, faster cooling implies stronger red-shifts).

The blue-shifted lines, however, are due to chromospheric ablation as excess heat flux from the corona impinges on and delivers energy to the chromosphere, ultimately causing an upwards expansion. So, why then should the up-flows be stronger for slower cooling (slower down-flows)? It appears to be a masking effect, in that the stronger blue-shifts have very weak intensities (see figure 5-7), and would almost certainly be below the detection threshold of Hinode-EIS (incidentally, no such trend occurs for the red-shifted lines). The loops which have the shortest cooling times are the ones which maintain their maximum temperature for long periods of time (reaching and maintaining hydrostatic equilibrium, and thus high densities and small flows, which dominate the signal), while the longer cooling times are the ones which do not maintain the maximum temperature for very long, and thus never reach hydrostatic equilibrium. The densities, and therefore intensities, are much greater in the hotter strands, where the flows are weak, and it is these strands which dominate the signal at high temperatures.

There is another interesting (and easily observable) feature of the Doppler shifts of these lines: the temperature at which they switch from red- to blue-shifts (call it the crossing temperature). This crossing temperature also depends on the cooling time (see figure 5-8), as we

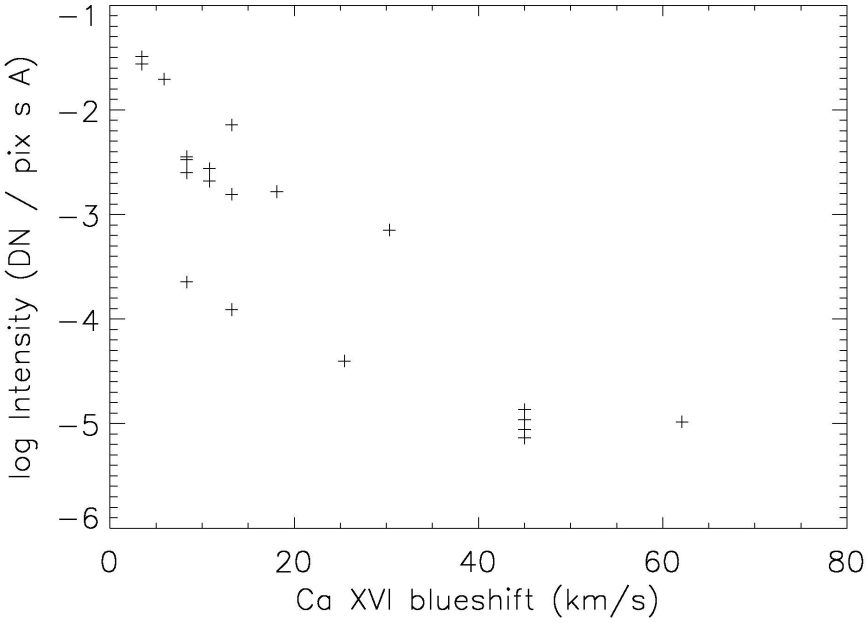

Figure 5-7: The blue-shift of the Ca XVI line for each simulation versus the (log of the) intensity for the same line. Note that the fastest moving ones have an intensity that would make the line essentially impossible to detect.

would expect. Note that the loops that cool faster (which are the loops with the longest heating events, see table 4) have a higher crossing temperature, and so the crossing temperature can used as a potential diagnostic for the heating of loops.

While we have not tried to reproduce any particular set of observations in this study, observational studies are in qualitative agreement with the predictions of this chapter. Teriaca *et al.* (1999 [64]; see figure 5-9) found red-shifts of around 10-15 km/s in the temperature range from about $10^{4.8}$ to $10^{5.70}$ K, with a crossing temperature around $10^{5.70}$

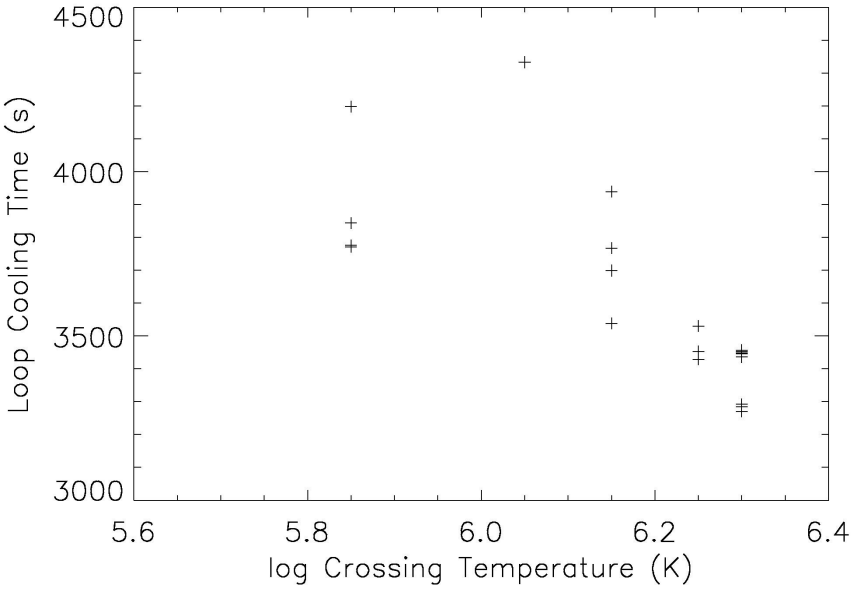

Figure 5-8: The temperature at which the lines switch from red- to blue-shifts versus the total cooling time of the loop.

K, where they found a few lines blue-shifted. The aforementioned study by Tripathi *et al.* (2009 [66]) found blue-shifts around 5-10 km/s up to $10^{6.4}$ K, with a crossing temperature around $10^{5.9}$ K. Doschek *et al.* (2008 [21]) find similar values of both blue- and red-shifted ions using Hinode-EIS, and interestingly find a strong correlation between the Doppler shifts and non-thermal velocities.

For repeating nanoflare storms, we thus expect to see red-shifts in the cooler ions on the order of 10 km/s. For loops that are heated for longer periods of time (reaching higher densities and attaining hydrostatic equilibrium), we also expect blue-shifts of the same order in the

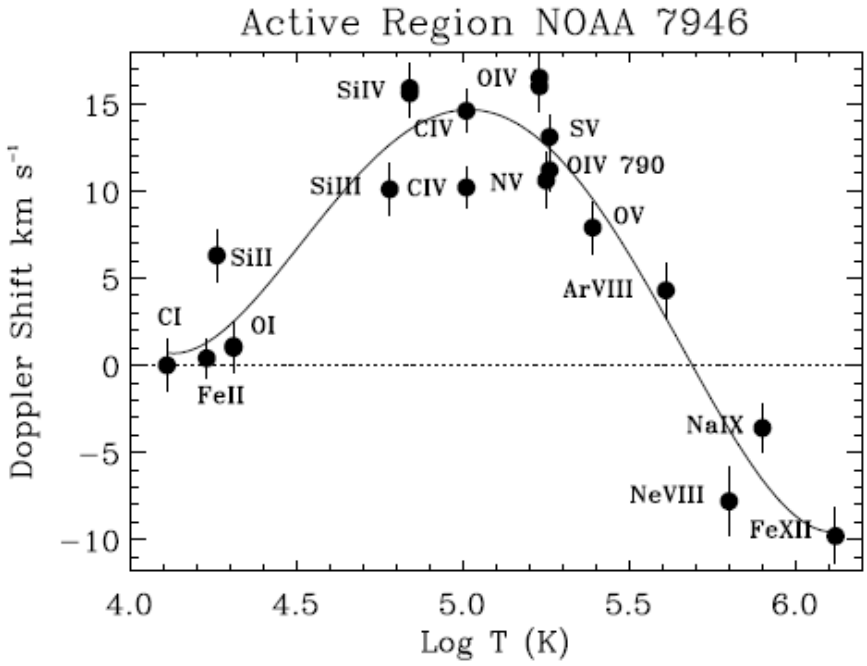

Figure 5-9: The Doppler shift velocities of an active region, measured with SOHO-SUMER. Taken from Teriaca *et al.* 1999 [64].

hotter ions. For loops that are heated for shorter periods of time, the blue-shifts may be stronger, but their intensities will likely be too weak for detection above the background. If we can calculate the cooling time of a loop (primarily a function of loop length), then we can also predict what temperature the lines will switch from being red-shifted to blue-shifted, which might also indicate how strong the heating is. Thus, we have a number of observables that can be readily checked.

In summary, we have demonstrated that repeating nanoflare storms can explain both the properties of the emission measure and the flow patterns. The results of our simulations are in qualitative agreement

with a number of published observational studies, although we have not tried to reproduce any given study.

6 Conclusions

6.1 Summary and Interpretations

In chapter 3, we examined heating of a coronal loop through a single heating event, lasting up to ten minutes. From the six simulations performed there, we found that the power-law index b of the true emission measure was significantly smaller than observational studies of similar active region loops. The index b_{Pot} calculated using the Pottasch method for lines seen with Hinode-EIS was found to be greater than the true power-law index b, but in general still smaller than those reported by observers. We suggested that the discrepancy was due to the heating mechanism adopted: a single heating event is insufficient to explain the distribution of plasma temperatures.

We thus turned to a mechanism of repeated heating events in chapter 4, in which individual strands are re-energized. We performed twenty numerical simulations this time, varying the number of heating events, as well as the heating and inter-event cooling times. This time we found a positive correlation between the ratio of heating time to cooling time and the power-law index b. We also found that the Pottasch indices were systematically stronger than the true emission

measure indices, and argued that this bias is due to a poor estimate of the density when calculating the contribution functions of the emission lines. We showed how this can be corrected by adjusting n so that the density-sensitive lines are brought into agreement with the less sensitive lines.

Our findings from both of these chapters essentially point to the same conclusion: coronal loops in active regions are impulsively heated. When a heating event is isolated in time (as in chapter 3 or the low-frequency simulation of Warren *et al.* 2011 [74]), there will be both excessive amounts of plasma at higher and lower temperatures than the peak of the emission measure. When the heating event is isolated temporally, the loop density will be fairly low, so the temperature will rise rapidly with the onset of heating (resulting in excessive high temperature plasma relative to the low temperature plasma). The temperature of the peak of the emission measure will not be maintained for very long before the loop begins to cool, and so the proportion of lower temperature plasma increases relative to that at higher temperatures.

However, when a heating event is repeated shortly after the first ceases on a particular strand, it will be more dense than it was initially (due to chromospheric ablation) and the temperature will not rise as

sharply. With each successive heating event, the multi-stranded loop will eventually find a mean temperature (corresponding to the peak of the emission measure) which can be maintained for a long period of time. Because the highest temperatures are only reached during the first heating event, there will be very little plasma above the peak. Further, because the peak temperature is maintained for a longer time than it would be with an individual event, there will be less low temperature plasma relative to the peak. The net result is that an impulsive heating mechanism shows strong agreement with the observed emission measures.

In addition, there are flows (both up- and down-flows) observed in active region coronal loops. From our synthesized Hinode-EIS spectra, we find that the cooler lines tend to be red-shifted on the order of 10 km/s. The blue-shifted lines (from chromospheric ablation) can be extremely fast ($\sim$ 50 km/s), but they tend to have significantly less intensity the faster they are (and thus much harder to see above the background). Blue-shifted lines on the order of 10 km/s, however, should be readily observable. Finally, the crossing temperature (that is, the temperature at which the lines switch from red- to blue-shifts) appears to be correlated with the cooling time of the loops, which in turn

is primarily a function of loop length, and so should be readily observable. The values found in our simulations are in qualitative agreement with published observational studies.

6.2 Future Work

There are a number of goals regarding future work. We have suggested that the heating of active region coronal loops is likely impulsive, in the form of repeating nanoflare storms. However, we have not examined in detail the effects of the recharging time of energy release (essentially the ratio $\frac{\tau_H}{\tau_C}$ in table 3). In other words, we have determined that the ratio of total heating to total cooling times is important, but what about the length of time of each individual storm? In our simulations, we have assumed *a priori* that each repeat of a nanoflare storm has the same duration, strength, and intermittent cooling period. However, that is only a simplification to our calculations; there is no reason to expect that real nanoflares would follow such a pattern.

Suppose that the energy release were due to magnetic reconnection, as the field lines become twisted due to convective motions on the surface. If the motions do not vary too drastically in terms of speed or strength, it would seem reasonable that the storage of energy

in the magnetic field be proportional to the amount of time between reconnection events (see Parker 1988 [51]). We cannot predict when reconnection will occur, but we can put constraints on the time between events. We have seen from chapter 3 that a single, temporally isolated heating event is insufficient to explain the distribution of plasma temperatures in an active region loop and can thus place an upper limit of time in between events as the time it would take to significantly cool a loop. From this reasoning, a suitable next step in our studies would be to distribute a number of heating events randomly in time (up to the total cooling time), with the volumetric heating rate proportional to the time since the last event. As briefly noted earlier, using the work of Viall & Klimchuk (2012 [73]), we may be able to diagnose the periodicity and length of the individual heating and cooling times.

We also would like to synthesize emission measures for predicting the results of satellites other than Hinode-EIS (for example, SDO-AIA). We could then compare our results with more observational studies than we can with the current work. Further, we have argued that the observational steepening of the power-law index b is due to poor choice of density when calculating the contribution functions of the emission lines. Perhaps there are other observational biases that we have not yet

identified that analysis with another satellite might pick up, or perhaps there are peculiarities of EIS' response that cause it to have a bias not present in other instruments.

The Doppler shifts of the spectral lines also provide significant clues into the heating mechanism. The crossing temperature, for example, may indicate the approximate strength of the heating. Our heating mechanism makes other predictions which can be readily checked against observations. However, the cooling time (correlated to crossing temperature, red-shifts, and blue-shifts) depends strongly on the loop length, which was not varied in the current work. Further, the individual heating and cooling times also contribute to these observables, and so varying them may also change our predictions. We can gain insight into the heating of coronal loops through careful study of all of these.

References

[1] Alexander, D. *The Sun.* Greenwood Guides to the Universe, Greenwood Press, 2009.

[2] Alfvén, H. *On Sunspots and the Solar Cycle.* Arkiv. f. Mat., Astron. o. Fys., vol. 29A (12), p. 1-17, 1943.

[3] Alfvén, H. *Granulation, Magneto-Hydrodynamic Waves, and the Heating of the Solar Corona.* Monthly Notices of the Royal Astronomical Society, vol. 107, p. 211, 1947.

[4] Aschwanden, M. & Nightingale, R. *Elementary Loop Structures in the Solar Corona Analyzed from TRACE Triple-Filter Images.* Astrophysical Journal, vol. 633, issue 1, p. 499-517, 2005.

[5] Aschwanden, M. & Sandman, A. *Bootstrapping the coronal magnetic field with STEREO: Unipolar Potential Field Modeling.* Astronomical Journal, vol. 140, issue 3, p.723-34, 2010.

[6] Berton, R. & Sakurai, T. *Stereoscopic determination of the three-dimensional geometry of coronal magnetic loops.* Solar Physics, vol. 96, p. 93-111, 1985.

[7] Bowen, I.S. *The Low Terms in Mn V and Fe VI.* Physical Review, vol. 47, issue 12, p.924-5, 1935.

[8] Bowen, I.S. & Edlén, B. *Forbidden Lines of Fe VII in the Spectrum of Nova RR Pictoris (1925).* Nature, vol. 143, issue 3618, p. 374, 1939.

[9] Bradshaw, S. & Mason, H. *A self-consistent treatment of radiation in coronal loop modeling.* Astronomy & Astrophysics, vol. 401, p. 699-709, 2003.

[10] Bradshaw, S. & Mason, H. *The radiative response of solar loop plasma subject to transient heating.* Astronomy & Astrophysics, vol. 407, p. 1127-38, 2003.

[11] Bradshaw, S. & Cargill, P. *The cooling of coronal plasmas.* Astronomy & Astrophysics, vol. 437, issue 1, p. 311-7, 2005.

[12] Bradshaw, S., & Cargill, P. *Explosive heating of low-density coronal plasma.* Astronomy & Astrophysics, vol. 458, issue 3, p.987-95, 2006.

[13] Bradshaw, S. & Cargill, P. *The Cooling of Coronal Plamsas. III. Enthalpy Transfer as a Mechanism for Energy Loss.* Astrophysical Journal, vol. 717, issue 1, p. 163-74, 2010.

[14] Bradshaw, S. & Klimchuk, J. *What dominates the coronal emission spectrum during the cycle of impulsive heating and cooling?* Astrophysical Journal Supplements, vol. 194, issue 26, 2011.

[15] Bruner, E.C. *The Lockheed OSO-8 program. Task 2: Analysis of data from the high resolution ultraviolet spectrometer experiment.* Final Report, 19 Nov. 1977-31 Aug. 1980 Lockheed Missiles and Space Co., Sunnyvale, CA. 1980.

[16] Cassak, P.A., Shay, M.A., & Drake, J.F. *Catastrophe Model for Fast Magnetic Reconnection Onset.* Physical Review Letters, vol. 95, issue 23, 2005.

[17] Del Zanna, G., & Mason, H.E. *Solar active regions: SOHO/CDS and TRACE observations of quiescent coronal loops.* Astronomy & Astrophysics, vol. 406, p. 1089-1103, 2003.

[18] Dere, K.P., *et al. CHIANTI - an atomic database for emission lines.* A & A Supplement Series, vol. 125, p. 149-73, 1997.

[19] Dere, K.P. *Ionization rate coefficients for the elements hydrogen through zinc.* Astronomy & Astrophysics, vol. 466, issue 2, p. 771-92, 2007.

[20] Di Matteo, V., *et al. Analysis and comparison of loop structures imaged with NIXT and Yohkoh/SXT.* Astronomy and Astrophysics, vol. 342, p.563-74, 1999.

[21] Doschek, G., *et al. Flows and Nonthermal Velocities in Solar Active Regions Observed with the EUV Imaging Spectrometer on Hinode: A Tracer of Active Region Sources of Heliospheric Magnetic Fields?* Astrophysical Journal, vol. 686, issue 2, p. 1362-71, 2008.

[22] Dulk, G.A. & McLean, D.J. *Coronal magnetic fields.* Solar Physics, vol. 57, p. 279-95, 1978.

[23] Edlén, Bengt. *Zur Kenntnis der Cl I-ähnlichen Spektren Cl I, A II, K III, Ca IV, Ti VI, V VII, Cr VIII, MN IX, Fe X und Co XI.* Zeitschrift für Physik, vol. 104, issue 5-6, p. 407-16, 1937.

[24] Edlén, Bengt. *An attempt to identify the emission lines in the spectrum of the solar corona.* Arkiv. mat. astron. fysik 28B, 1, 1941. Reproduced in: *A source book in astronomy and astrophysics 1900-1975.* Cambridge, Mass.: Harvard University Press 1979.

[25] Feldman, U., *et al. The potential for plasma diagnostics from stellar extreme-ultraviolet observations.* Astrophysical Journal Supplement Series, vol. 81, no. 1, p. 387-408, 1992.

[26] Feng, L., *et al. First Stereoscopic Coronal Loop Reconstructions from STEREO SECCHI Images.* Astrophysical Journal, vol. 671, issue 2, p. L205-8, 2007.

[27] Gary, G. Allen. *Plasma Beta above a Solar Active Region: Rethinking the Paradigm.* Solar Physics, vol. 203, issue 1, p. 71-86. 2001.

[28] Goedbloed, Hans & Poedts, Stefaan. *Principles of Magnetohydrodynamics.* Cambridge University Press, 2004.

[29] Golub, L., *et al. Magnetic fields and coronal heating.* Astrophysical Journal, part 1, vol. 238, p. 343-8. 1980.

[30] Golub, L. & Herant, M. *Analysis of the 23 June 1988 flare using NIXT multilayer X-ray images.* In: X-ray/EUV optics for astronomy and microscopy; Proceedings of the Meeting, San Diego, CA, Aug. 7-11, 1989. Bellingham, WA, Society of Photo-Optical Engineers, 1989, p. 629-35.

[31] Golub, Leon & Pasachoff, Jay M. *The Solar Corona.* 2nd Edition, Cambridge University Press, 2010.

[32] Grotrian, W. *Sonne und Ionosphäre.* Die Naturwissenschaften, vol. 27, issue 33, p. 555-63, 1939.

[33] Hunter, A. *Origin of the Coronium Lines.* Nature, vol. 150, issue 3817, p. 756-9, 1942.

[34] Jones, H. Spencer. *Nova RR Pictoris (1925), The spectrum of, in 1933.* Monthly Notices of the Royal Astronomical Society, Vol. 94, p.35-9, 1933.

[35] Jordan, C. *The structure of solar active regions from EUV and soft X-ray observations.* In: Solar gamma-, X-, and EUV radiation; Proceedings of the Symposium, Buenos Aires, Argentina, June 11-14, 1974. Dordrecht, D. Reidel Publishing Co., 1975.

[36] Jordan, C. *The energy balance of the solar transition region.* Astronomy & Astrophysics, vol. 86, no. 3, p. 355-63, 1980.

[37] Jordan, C., *et al. The chromospheres and coronae of five G-K main-sequence stars.* Monthly Notices of the Royal Astronomical Society, vol. 225, p. 903-37, 1987.

[38] Kaiser, M.L., *et al. The STEREO Mission: An Introduction.* Space Science Reviews, vol. 136, issue 1-4, p.5-16, 2008.

[39] Klimchuk, J., *et al. Thickness variations along coronal loops observed by the Soft X-ray Telescope on YOHKOH.* Publications of the Astronomical Society of Japan, vol. 44, no. 5, p. L181-5, 1992.

[40] Klimchuk, James. *On Solving the Coronal Heating Problem.* Solar Physics, vol. 234, issue 1, p. 41-77. 2006.

[41] Landi, E., *et al. CHIANTI - An Atomic Database for Emission Lines. XII. Version 7 of the Database.* Astrophysical Journal, vol. 744, issue 2, p. L99-107, 2012.

[42] Lin, R.P., Schwartz, R.A., & Kane, S.R. *Solar Hard X-ray Microflares.* Astrophysical Journal, vol. 283, p.421-5, 1984.

[43] Lyot, Bernard. *La couronne solaire étudiée en dehors des éclipses.* Bulletin Astronomique, vol. 6, p. 305-16. 1930.

[44] Lyot, Bernard. *A Study of the Solar Corona and Prominences without Eclipses.* Monthly Notices of the Royal Astronomical Society, vol. 99, p.580. (George Darwin Lecture, 1939).

[45] Martens, P.C.H., Kankelborg, C.C., & Berger, T.E. *On the Nature of the "Moss" Observed by TRACE.* Astrophysical Journal, vol. 537, issue 1, p.471-80, 2000.

[46] Martinez-Sykora, J., *et al. What do spectral line profile asymmetries tell us about the solar atmosphere?* Astrophysical Journal, vol. 732, p.84, 2011.

[47] Mazzotta, P., *et al. Ionization balance for optically thin plasmas: Rate coefficients for all atoms and ions of the elements H to Ni.* Astronomy & Astrophysics Supplement, vol. 133, p. 403-9, 1998.

[48] Mitchell, S.A. *Eclipses of the Sun.* Columbia University Press, 3rd edition, 1932.

[49] Ossendrijver, Mathieu. *The solar dynamo.* The Astronomy and Astrophysics Review, vol. 11, issue 4, p. 287-367. 2003.

[50] Parker, E.N. *Sweet's Mechanism for Merging Magnetic Fields in Conducting Fluids.* Journal of Geophysical Research, vol. 62, issue 4, p. 509-20, 1958.

[51] Parker, E.N. *Nanoflares and the Solar X-ray Corona.* Astrophysical Journal, vol. 330, p. 474-9, 1988.

[52] Petschek, H.E. *Magnetic Field Annihilation.* The Physics of Solar Flares, Proceedings of the AAS-NASA Symposium held 28-30 October, 1963 at the Goddard Space Flight Center, Greenbelt, MD. NASA, Science and Technical Information Division, 1964.

[53] Pottasch, S. *The lower solar corona: Interpretation of the ultraviolet spectrum.* Astrophysical Journal, vol. 137, p. 945-66, 1963.

[54] Priest, E. *Solar Magnetohydronamics.* D. Reidel Publishing, 3rd edition, 1987.

[55] Priest, E. & Forbes, T. *Magnetic Reconnection: MHD Theory and Applications.* Cambridge University Press, 2000.

[56] Reale, F. & Orlando, S. *Nonequilibrium of ionization and the detection of hot plasma in nanoflare-heated coronal loops.* Astrophysical Journal, vol. 684, p.715-24, 2008.

[57] Reale, F. *Coronal Loops: Observations and Modeling of Confined Plasma.* Living Reviews in Solar Physics, vol. 7, no. 5, 2010.

[58] Rosner, R., Tucker, W.H., & Vaiana, G.S. *Dynamics of the quiescent solar corona.* Astrophysical Journal, part 1, vol. 220, p. 643-5, 647, 649-53, 655-65. 1978.

[59] Rybicki, George & Lightman, Alan. *Radiative Processes in Astrophysics.* John Wiley & Sons, Inc., 1979.

[60] Schwarzschild, M. *On Noise Arising from the Solar Granulation.* Astrophysical Journal, vol. 107, p. 1, 1948.

[61] Sonnerup, B. *Magnetic-field re-connexion in a highly conducting incompressible fluid.* Journal of Plasma Physics, vol. 4, issue 1, p. 161, 1970.

[62] Stein, R.F. & Leibacher, J. *Waves in the solar atmosphere.* Annual review of astronomy and astrophysics, vol. 12, p. 407-35, 1974.

[63] Sweet, P.A. *The Neutral Point Theory of Solar Flares.* Electromagnetic Phenomena in Cosmical Physics, Proceedings from IAU Symposium no. 6. Cambridge University Press, 1958.

[64] Teriaca, L., *et al. SUMER observations of Doppler shift in the quiet Sun and in an active region.* Astronomy & Astrophysics, vol. 349, p. 636-48, 1999.

[65] Tomczyk, S., *et al. An Instrument to Measure Coronal Emission Line Polarization.* Solar Physics, vol. 247, issue 2, p. 411-28, 2008.

[66] Tripathi, D., *et al. Active Region Loops: Hinode/Extreme-Ultraviolet Imaging Spectrometer Observations.* Astrophysical Journal, vol. 694, p.1256-65, 2009.

[67] Tripathi, D., Klimchuk, J., & Mason, H. *Emission Measure Distribution and Heating of Two Active Region Cores.* Astrophysical Journal, vol. 740, p.111-20, 2011.

[68] Tucker, W. & Koren, M. *Radiation from a High-Temperature Low-Density Plasma: the X-Ray Spectrum of the Solar Corona.* Astrophysical Journal, vol. 168, p. 283, 1971.

[69] Tucker, W. & Koren, M. *Erratum: Radiation from a High-Temperature Low-Density Plasma: the X-Ray Spectrum of the Solar Corona.* Astrophysical Journal, vol. 170, p. 170, 1971.

[70] Vaiana, G.S., Krieger, A.S., & Timothy, A.F. *Identification and Analysis of Structures in the Corona from X-Ray Photography.* Solar Physics, vol. 32, issue 1, p. 81-116, 1973.

[71] van SpeyBroeck, L.P., Krieger, A.S., & Vaiana G.S. *X-ray photographs of the sun on March 7, 1970.* Nature, vol. 227, issue 5260, p. 818-22, 1970.

[72] Velli, M. & Pruneti, F. *Alfvén waves in the solar corona and solar wind.* Plasma Physics and Controlled Fusion, vol. 39, number 12B, 1997.

[73] Viall, N. & Klimchuk, J. *Evidence for Widespread Cooling in an Active Region Observed with the SDO Atmospheric Imaging Assembly.* arXiv:1202.4001v1, 2012.

[74] Warren, H., Brooks, D., & Winebarger, A. *Constraints on the Heating of High-Temperature Active Region Loops: Observations from Hinode and the Solar Dynamics Observatory.* Astrophysical Journal, vol. 734, p. 90, 2011.

[75] Whitaker, W. *Heating of the Solar Corona by Gravity Waves.* Astrophysical Journal, vol. 137, p. 914, 1963.

[76] Winebarger, A. & Warren, H. *Can TRACE extreme-ultraviolet observations of cooling coronal loops be used to determine the heating parameters?* Astrophysical Journal, vol. 610, L129-32, 2004.

[77] Winebarger, A. & Warren, H. *Cooling Active Region Loops Observed with SXT and TRACE.* Astrophysical Journal, vol. 626, issue 1, p. 543-50, 2005.

[78] Winebarger, A., *et al. Using a Differential Emission Measure and Density Measurements in an Active Region Core to Test a Steady Heating Model.* Astrophysical Journal, vol. 740, issue 1, 2011.

[79] Yamada, M., *et al. Experimental investigation of the neutral sheet profile during magnetic reconnection.* Physics of Plasmas, vol. 7, issue 5, p. 1781-7, 2000.

[80] Yamada, M., Kulsrud, R., & Ji, H. *Magnetic reconnection.* Reviews of Modern Physics, vol. 82, issue 1, p. 603-64, 2010.

[81] Yeh, T. & Axford, W.I. *On the re-connexion of magnetic field lines in conducting fluids.* Journal of Plasma Physics, vol. 4, p. 207, 1970.

[82] Young, C.A. *The Corona Line*. Nature, Vol. 7, issue 159, p.28, 1872.